Available online at www.sciencedirect.com
SCIENCE DIRECT®
Journal of Computational Physics 199 (2004) 376–422
JOURNAL OF COMPUTATIONAL PHYSICS
www.elsevier.com/locate/jcp

Rapid evaluation of radiation boundary kernels for time-domain wave propagation on blackholes: theory and numerical methods ☆

Stephen R. Lau [1]

Applied Mathematics Group, Department of Mathematics, CB #3250, Phillips Hall, University of North Carolina, Chapel Hill, NC 27599-3250, USA

Received 26 January 2004; received in revised form 1 April 2004; accepted 11 May 2004
Available online 8 July 2004

Abstract

For scalar, electromagnetic, or gravitational wave propagation on a fixed Schwarzschild blackhole background, we describe the exact nonlocal radiation outer boundary conditions (ROBC) appropriate for a spherical outer boundary of finite radius enclosing the blackhole. Derivation of the ROBC is based on Laplace and spherical-harmonic transformation of the *Regge–Wheeler equation*, the PDE governing the wave propagation, with the resulting radial ODE an incarnation of the *confluent Heun equation*. For a given angular index l the ROBC feature integral convolution between a time-domain radiation boundary kernel (TDRK) and each of the corresponding $2l + 1$ spherical-harmonic modes of the radiation field. The TDRK is the inverse Laplace transform of a frequency-domain radiation kernel (FDRK) which is essentially the logarithmic derivative of the asymptotically outgoing solution to the radial ODE. We develop several numerical methods for examining the frequency dependence of both the outgoing solution and the FDRK. Using these methods we numerically implement the ROBC in a follow-up article. Our work is a partial generalization to Schwarzschild wave propagation and Heun functions of the methods developed for flatspace wave propagation and Bessel functions by Alpert, Greengard, and Hagstrom (AGH), save for one key difference. Whereas AGH had the usual armamentarium of analytical results (asymptotics, order recursion relations, bispectrality) for Bessel functions at their disposal, what we need to know about Heun functions must be gathered numerically as relatively less is known about them.

☆ Drawn from [1].

E-mail address: lau@email.unc.edu (S.R. Lau).
URL: www.unc.edu/~lau/.
[1] Present address: Center for Gravitational Wave Astronomy, University of Texas at Brownsville/Texas Southmost College, 80 Fort Brown, Brownsville, Texas 78520, USA.

0021-9991/$ - see front matter © 2004 Elsevier Inc. All rights reserved.
doi:10.1016/j.jcp.2004.05.013

1. Introduction

This article is essentially the first half of [1], while a follow-up article [2], submitted elsewhere, is the second half. Although we occasionally mention results from [1,2], this article is completely self-contained.

1.1. Background

Consider the Cauchy problem [2] for the scalar wave equation,

$$-\partial_t^2 U + \Delta U = 0, \tag{1}$$

on $[t_0, t_F] \times \mathbb{E}^3$, the Cartesian product of a closed time interval and Euclidean three-space. First, we specify suitable initial-value or canonical data $U|_{t_0}$ and $\partial_t U|_{t_0}$ on $\mathbb{E}^3$ at the initial time t_0. Next, using the rule (1), we evolve the data until the final time t_F, along the way generating the solution U throughout the temporally bounded but spatially unbounded domain $[t_0, t_F] \times \mathbb{E}^3$. Provided physically reasonable initial data, this problem is well-posed; however, it is not the evolution problem one typically encounters in numerical wave simulation. Usually the numerical mesh covers only a *finite* portion of $\mathbb{E}^3$.

With the finiteness of numerical meshes in mind, consider the following more realistic evolution problem. Let $\Sigma \subset \mathbb{E}^3$ be a round, solid, three-dimensional ball determined by $r \leqslant r_B$, with r_B a fixed outer radius, on which we specify compactly supported initial data $U|_{t_0}$ and $\partial_t U|_{t_0}$ at $t = t_0$. Again, the goal is to evolve the data, although now generating the solution U on the finite domain $\mathscr{M} = [t_0, t_F] \times \Sigma$ depicted in Fig. 1. Respectively, let Σ_0 and Σ_F denote the ball Σ at $t = t_0$ and $t = t_F$. One element of the boundary $\partial\mathscr{M} = \Sigma_0 \cup \Sigma_F \cup {}^3B$ is a timelike three-dimensional cylinder ${}^3B$ determined by $t_0 \leqslant t \leqslant t_F$ and $r = r_B$. Note that ${}^3B$ is the history in time of the spherical spatial boundary $B = \partial\Sigma$. As it stands, such an evolution problem is not well-posed, since $\mathscr{M}$ is larger than the future domain of dependence of Σ_0. Indeed, $U|_{t_0}$ and $\partial_t U|_{t_0}$ are *free data*, and we have no control over data on $\mathbb{E}^3/\Sigma_{\mathbb{O}}$, the region exterior to the initial Σ ball. Data on this exterior region may contain so-called ingoing radiation which will impinge upon ${}^3B$ at later times, affecting the solution U within $\mathscr{M}$. Most often in numerical wave simulation the goal is to forbid such ingoing radiation by the choice of *radiation boundary conditions*, that is explicit rules governing the behavior of U and $\partial_t U$ on ${}^3B$. Often referred to as *nonreflecting boundary conditions* (NRBC), for the described problem such conditions ideally specify that the spherical boundary B is completely transparent. Due to the free nature of the initial data, *exact* NRBC are inherently nonlocal in both space and time. With NRBC specified along ${}^3B$, we may refer to such an evolution as a *mixed Cauchy-boundary value problem*.

More generally, one might consider radiation boundary conditions associated with some other PDE and/or different type of B boundary, say cubical or irregularly shaped. Refs. [5–21] pertain either to the described spherical problem or to more general radiation boundary conditions. This is certainly not an exhaustive list, and we point the reader to review articles [12,18,21] for more comprehensive listings. Although we do not attempt an extensive literature review, we make mention of a few approaches to radiation boundary conditions in order to put our work in some context. Two pioneering early works are those of Engquist and Majda [6,7] and Bayliss and Turkel [9]. Each develops a hierarchy of *local* differential conditions of increasing complexity. Engquist and Majda's work is based on exact radiation boundary conditions as expressed within the theory of pseudo-differential operators, and their approach is not necessarily tied to a spherical geometry nor to the ordinary wave equation. Also considering more

[2] We use *Cauchy problem* in lieu of *initial-value problem* in order to reserve the latter for the process of generating initial data, one that requires the solution of elliptic PDE for theories involving constraints such as general relativity or fluid flow.

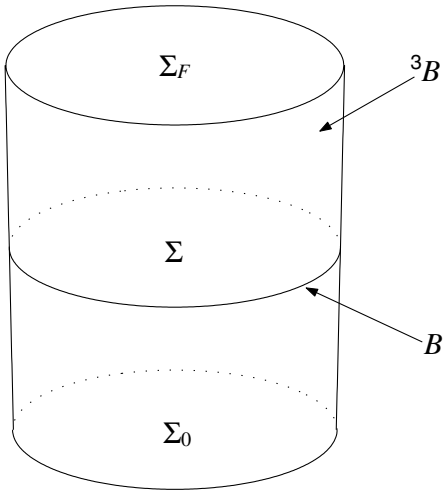

Fig. 1. Finite spacetime domain $\mathscr{M} \subset \mathbb{E}^3$ with boundary $\partial\mathscr{M} = \Sigma_0 \cup \Sigma_F \cup {}^3B$. Respectively, Σ_0 and Σ_F denote the solid round ball Σ at the initial time t_0 and the final time t_F. Radiation boundary conditions are given on the three-dimensional timelike cylinder ^3B. Our geometric perspective on the "quasilocal" spacetime region $\mathscr{M}$ comes from [3,4].

than just our problem above, Bayliss and Turkel base their approach on asymptotic expansions about infinity, for example the standard multipole expansion for a radiating field obeying the ordinary wave equation (1). Another approach to radiation boundary conditions utilizes absorbing layers, and as an example we mention [11]. In the introduction of his review article [18], Hagstrom describes the main advances made in the 1990s on several fronts related to radiation boundary conditions: (i) improved implementations of hierarchies, such as the ones mentioned, (ii) new absorbing layer techniques exhibiting reflectionless interfaces, and (iii) efficient algorithms for evaluation of exact nonlocal boundary operators. Results [15–17] of Grote and Keller fall within this first category. An advance on the second front was the introduction of *perfectly matched layers* by Bérenger [14], while a key advance on the third was the rapid implementation of NRBC for spherical boundaries by Alpert et al. [19,20]. See also related work by Sofronov [13]. Hagstrom discusses the state of the art for fronts (ii) and (iii) in his second review article [21].

Since our investigation follows that of Alpert, Greengard, and Hagstrom (AGH) belonging to category (iii) in the last paragraph, let us describe it in detail. Taking advantage of the linearity, time-independence, and rotational invariance of (1), AGH employ both Laplace and spherical-harmonic transformation in order to obtain a second-order radial ODE (the modified spherical Bessel equation). Working in the frequency-domain with the two linearly independent solutions to this ODE, they are able to determine the correct form of a radiating solution, provided that they examine the said solution at a radial location beyond the support of the initial data. Via inverse Laplace transformation of the radial derivative of this correct frequency-domain solution, they then introduce a *nonreflecting boundary kernel*, here called a *time-domain radiation kernel* (TDRK). The TDRK is the inverse Laplace transform of a *frequency-domain radiation kernel* (FDRK) which is essentially the logarithmic derivative of a modified Bessel function. To sharpen this statement, first consider the standard half-integer order *MacDonald function* [22] $K_{l+1/2}(z)$ with angular index l, and also the associated function $W_l(z) = (\pi z/2)^{1/2} \exp(z) K_{l+1/2}(z)$ more closely related to a confluent hypergeometric function. Here $z = sr$ is shorthand for the product of Laplace frequency s and radius r. In terms of the fixed outer boundary radius r_B, the TDRK for angular index l is the inverse Laplace transform of the FDRK $sr_B W_l'(sr_B)/W_l(sr_B)$. Such a logarithmic derivative is a sum of l simple

poles in the complex s-plane, whence its inverse Laplace transform is a corresponding sum of exponentials. [3] AGH also employ an algorithm for kernel compression, that is rational approximation of the FDRK. We comment on this algorithm in Section 2.4.2, and describe it in detail in both [1,2].

1.2. Problem statement

Now consider the evolution problem for the scalar wave equation,

$$\sum_{\mu,\nu=0}^{3} \frac{1}{\sqrt{-g}} \frac{\partial}{\partial x^{\mu}} \left(\sqrt{-g} g^{\mu\nu} \frac{\partial U}{\partial x^{\nu}} \right) = 0, \tag{2}$$

describing a field U propagating on a Schwarzschild blackhole determined by $g_{\mu\nu}$ metric functions. A slight modification of (2) yields a wave equation flexible enough to also describe propagation of electromagnetic or gravitational waves on a Schwarzschild blackhole [24–27]. As a model of gravitational wave propagation, the problem has applications in relativistic astrophysics: non-spherical gravitational collapse and stellar perturbations, among others. Gravitational wave propagation is also of considerable theoretical interest in general relativity. With numerical wave simulation on a finite mesh in mind, we again choose a finite domain Σ, now a round, three-dimensional, thick shell also bounded internally by the blackhole horizon H. The outer boundary B, one element of $\partial\Sigma = B \cup H$, is again specified by $r = r_{\mathrm{B}}$, while the inner boundary H corresponds to $r = 2\mathrm{m}$ (twice the geometrical mass of the blackhole). Let us set the task of evolving data $U|_{t_0}$ and $\partial_t U|_{t_0}$ given on Σ_0, in order to generate the solution U on the finite domain $\mathscr{M} = [t_0, t_{\mathrm{F}}] \times \Sigma$ with boundary $\partial\mathscr{M} = \Sigma_0 \cup \Sigma_{\mathrm{F}} \cup {}^3B \cup {}^3H$. [4] Here ${}^3H$, a portion of the *future event horizon*, is the three-dimensional characteristic history $[t_0, t_{\mathrm{F}}] \times H$ of H. To accomplish the task, we need explicit outer boundary conditions on ${}^3B = [t_0, t_{\mathrm{F}}] \times B$, ones stemming from the assumption of trivial initial data on the outer spatial region exterior to Σ_0. We refer to these as *radiation outer boundary conditions* (ROBC). [5] The ROBC corresponding to (2) are more subtle than simple nonreflection, in part due to the back-scattering of waves off of curvature.

In discussing *finite* outer boundary conditions, and ROBC in particular, for relativity, we should first make a distinction between general relativity, in which the dynamics of spacetime is governed by the full nonlinear Einstein equations, and its perturbation theory, in which the dynamics of disturbances on a fixed background solution to the Einstein equations is governed by a linear PDE similar to (2). In this second paradigm one examines the propagation of weak gravitational waves on a fixed background spacetime (which may or may not be curved). York's survey article [28] on the dynamics and kinematics of general relativity is the best jumping off point for a study of the literature we now mention. Within the context of a mixed Cauchy-boundary value problem, Friedrich and Nagy have made theoretical progress towards solving the full Einstein equations on a bounded domain [29]; however, their results do not appear suited for numerical work. For the most part, approaches towards numerical outer boundary conditions in the full theory have relied either on matching Cauchy domains to characteristic surfaces (see [30,31] and references therein) or ensuring that the outer boundary is at a large enough distance so that perturbation theory can be brought into play (see [32,33] and reference therein). In this latter approach, the relevant perturbative

[3] Domain reduction appears in the early work [8] of Gustafsson and Kreiss, although domain reduction via Laplace convolution appears shortly thereafter in the work [10] of Hagstrom. In [23] Friedlander considered essentially the same convolution kernel but in a different context.

[4] Although it hardly needs to be noted now, our time t here is closely related to the advanced Eddington–Finkelstein coordinate v discussed in the follow-up article [2]. We could also work with the static time T introduced in Section 2.1.1.

[5] Our acronym includes the adjective "outer" in order to distinguish between boundary conditions at B and those at H. Setting appropriate boundary conditions at H is not nearly so difficult for our problem, since H acts as a one-way membrane. However, for dynamical spacetimes the issue of inner boundary conditions (at "apparent horizons") is a difficult problem in its own right.

wave equation is essentially (2); however, the corresponding exact nonlocal ROBC are not used. A very different approach towards theoretical and numerical outer boundary conditions has been given in [34]. However, it would seem of limited practical use, since it relies on the "many-fingered" nature of time in general relativity to completely freeze the flow of time at the outer boundary. In terms of harmonic coordinates Szilágyi, Schmidt, and Winicour have theoretically and numerically studied mixed Cauchy-boundary value problems for the Einstein equations linearized about flat Minkowski spacetime [35]. Attempts towards implementation of ROBC in numerical relativity have mostly relied on improved versions of the well-known Sommerfeld condition, although Novak and Bonazzola have considered more general nonreflecting boundary conditions with relativistic applications in mind [36]. The Sommerfeld condition is a local boundary condition which is exact for a spherically symmetric outgoing wave in flatspace. For comments on such approaches as well as other remarks on numerical relativity, see the review article by Cook and Teukolsky [37]. To date, there seems to have been no truly systematic analysis of algorithm error for treatments of ROBC in numerical relativity.

We use frequency-domain methods and gather results which resemble those used and found in seminal work [38] by Leaver and also in related work [39] by Andersson. Despite this resemblance, neither Leaver nor Andersson considered *boundary* integral kernels belonging to the finite timelike cylinder ${}^3B$. The starting point for these authors was the exact solution to the Cauchy problem as expressed via an integral (Green's function) representation involving Σ_0 *spatial* convolution with initial data (actually Leaver also considered more general driving source terms beyond just initial data). As Leaver noted in footnote 21 of [38], the seeds of this approach are found in Morse and Feshbach's 1953 treatment [40] of the ordinary flatspace wave equation, although they have origins in the 19th century. Many authors have since used frequency-domain and complex-analytic methods to examine the Cauchy problem for perturbations on the Schwarzschild geometry from this Green's function perspective, and Andersson's article [39] is a salient recent example. However, we stress up-front that our problem of imposing ROBC via domain reduction is not the same as Leaver and Andersson's problem, and our work has quite a different focus on ${}^3B$ *temporal* integral convolution. Moreover, the methods – those of AGH – that we describe and use in this article and its follow-up were only fully developed for the ordinary wave equation in the late 1990s. Section 2.4.3 further compares and contrasts our theoretical analysis with that of Leaver and Andersson.

1.3. Overview of results

In this article and its follow-up [2] we describe both the exact ROBC for (2) and an algorithm for their rapid numerical implementation. As mentioned, our approach follows AGH quite closely. Eq. (2) is linear, but necessarily with variable coefficients. Nevertheless, exploiting its time and rotational symmetries, we may likewise use Laplace and spherical-harmonic transformation in order to obtain a second-order radial ODE which turns out to be an incarnation of the *confluent Heun equation* [41,42], also related to the *generalized spheroidal wave equation* [6] discussed in some literature [43,44]. Following AGH, we may formally introduce the TDRK as the inverse Laplace transform of the homogeneous logarithmic derivative of the asymptotically outgoing solution. Analytically, the FDRK, the logarithmic derivative in question, is a sum of poles, although now the sum is over both a discrete set and a continuous set (similar to the situation encountered with the flatspace wave equation in $2+1$ rather than $3+1$ dimensions [19]). In this article we focus on both description of the ROBC as well as the numerical methods which justify this description. These numerical methods are also used to implement the ROBC in [2].

[6] The ordinary *spheroidal wave equation* stems from variable separation of the ordinary wave equation (1) in oblate or prolate spheroidal coordinates [40].

1.4. Summary

Section 2 discusses variable transformations, various resulting forms of (2), and the exact ROBC. We start off by defining dimensionless coordinates for time τ, radius ρ, and Laplace frequency σ. For example, $r = 2m\rho$ and $s = \sigma/(2m)$. The outer boundary B is determined $\rho = \rho_B$. With these coordinates we introduce the asymptotically outgoing solution $W_l(\sigma\rho;\sigma)$ to the radial equation, the one corresponding to the Bessel-type function $W_l(sr) = W_l(\sigma\rho)$ above. For a given angular index l the TDRK $\omega_l(\tau;\rho_B)$ is the inverse Laplace transform of the FDRK $\hat{\omega}_l(\sigma;\rho_B) = \sigma\rho_B W_l'(\sigma\rho_B;\sigma)/W_l(\sigma\rho_B;\sigma)$. We then write the ROBC as an integral convolution between $\omega_l(\tau;\rho_B)$ and each of the corresponding $2l+1$ modes $\psi_{lm}(\tau,\rho_B)$ of the radiating field $\psi(\tau,\rho,\theta,\phi)$, where ψ is U from above but expressed in terms of different coordinates. Afterwards, we describe the key representation of $\hat{\omega}_l(\sigma;\rho_B)$ as a (continuous and discrete) sum of poles. We also briefly touch upon the issue of approximating $\hat{\omega}_l(\sigma;\rho_B)$ by a rational function (a key technique used in the follow-up article [2]). Section 2 ends we a comparison between our theoretical analysis and the aforementioned Green's function perspective.

Section 3 describes numerical evaluation of both $W_l(\sigma\rho_B;\sigma)$ and $\hat{\omega}_l(\sigma;\rho_B)$, with the former considered as a function of complex Laplace frequency σ (mostly lying in the lefthalf plane) and the latter as a function of purely imaginary $\sigma = iy$. Both types of evaluation rely on numerical integration over certain paths in the complex plane. We consider several numerical methods, but the main ones involve path integration in terms of a complex variable $z = \sigma\rho$. While numerical evaluation of $W_l(\sigma\rho_B;\sigma)$ is important insofar as studying the analytic structure of this function is concerned, implementation of ROBC mainly requires that we are able to accurately evaluate $\hat{\omega}_l(iy;\rho_B)$ for any $y \in \mathbb{R}$. In this section we also discuss in detail the accuracy of our numerical methods.

Section 4 focuses on the sum-of-poles representations of $\hat{\omega}_l(\sigma;\rho_B)$. The first subsection is a qualitative description of the analytic structure of $W_l(\sigma\rho_B;\sigma)$ and its relevance for the exact sum-of-poles representation. This subsection examines the zeros in frequency σ of $W_l(\sigma\rho_B;\sigma)$ which correspond to poles of $\hat{\omega}_l(\sigma;\rho_B)$. It also studies the branch behavior of $W_l(\sigma\rho_B;\sigma)$ along the negative $\mathrm{Re}\,\sigma$ axis, behavior that gives rise to a continuous pole distribution (these are not really poles in the sense of complex analysis). This distribution appears in the exact sum-of-poles representation, and we graphically examine it. The second subsection presents our direct numerical construction of $\hat{\omega}_l(\sigma;\rho_B)$ for $0 \leqslant l \leqslant 10$ and $\rho_B \in [15,25]$. We discuss several numerical accuracy checks of our direct construction.

A discussion section compares our work that of AGH, our main reference [19].

Throughout this article we make use of the following acronyms:

ROBC	radiation outer boundary conditions
ODE	ordinary differential equation
PDE	partial differential equation
TDRK	time-domain radiation (boundary) kernel $\omega_l(\tau;\rho_B)$
FDRK	frequency-domain radiation (boundary) kernel $\hat{\omega}_l(\sigma;\rho_B)$
AGH	Alpert, Greengard, and Hagstrom in [19]
NRBC	nonreflecting boundary conditions (particular ROBC for flatspace waves)
MSBE	modified spherical Bessel equation
LHS	left-hand side
RHS	right-hand side

2. Wave equation and radiation outer boundary conditions

This section sets up the theoretical framework on which the subsequent sections in this article and the sequel rest.

2.1. Wave equation on Schwarzschild background

2.1.1. Line-element

Consider the diagonal line-element describing a static, spherically symmetric, vacuum blackhole of mass m,

$$ds^2 = -F\,dT^2 + F^{-1}\,dr^2 + r^2\,d\theta^2 + r^2\sin^2\theta\,d\phi^2, \tag{3}$$

written with respect to the standard static time T and areal radius r [45,46]. We use uppercase T here to save lowercase t for a different time coordinate needed later. Note that the metric coefficient $F(r) = 1 - 2m/r$ vanishes – and so F^{-1} is singular – as $r \to 2m$. As is well known, $r = 2m$ does not represent a physical singularity, rather the coordinate system is degenerate for this value of the radius. In these coordinates the round sphere determined by $r = 2m$ is the bifurcate cross-section of the event horizon of the blackhole. In this work, we are chiefly interested in the "exterior region" defined by $2m < r < \infty$.

It will prove convenient to pass to and work with dimensionless coordinates $(\tau, \rho, \theta, \phi)$ defined by

$$2m\tau = T, \quad 2m\rho = r \tag{4}$$

(θ and ϕ are already dimensionless). After the rescaling $ds^2 \mapsto ds^2/(4m^2)$, we may rewrite the line-element (3) in the dimensionless form

$$ds^2 = -F\,d\tau^2 + F^{-1}\,d\rho^2 + \rho^2\,d\theta^2 + \rho^2\sin^2\theta\,d\phi^2, \tag{5}$$

where now $F(\rho) = 1 - 1/\rho$ so the unphysical singularity is located at $\rho = 1$.

We also consider the outgoing and ingoing systems of Eddington–Finkelstein coordinates [45,46], here in dimensionless form. To construct them, first introduce the *Regge–Wheeler tortoise coordinate* [25,45]

$$\rho_* = \rho + \log(\rho - 1). \tag{6}$$

Recall that this transformation is valid for $1 < \rho < \infty$ which corresponds to $-\infty < \rho_* < \infty$, and that $\rho \to 1^+$ corresponds to $\rho_* \to -\infty$. The characteristic coordinate $\mu = \tau - \rho_*$ is the *retarded time*, and the set $(\mu, \rho, \theta, \phi)$ is the outgoing Eddington–Finkelstein system. With respect to it, the line-element takes the form

$$ds^2 = -F\,d\mu^2 - 2\,d\mu\,d\rho + \rho^2\,d\theta^2 + \rho^2\sin^2\theta\,d\phi^2. \tag{7}$$

In the $(\mu, \rho, \theta, \phi)$ system $g_{\rho\rho} = 0$, so that the vector field $\partial/\partial\rho$ is characteristic or *null*, whereas in the $(\tau, \rho, \theta, \phi)$ system $g_{\rho\rho} = F^{-1}(\rho)$, so that $\partial/\partial\rho$ is spacelike on the exterior region. Level-μ hypersurfaces are characteristic and outgoing (cones opening towards the future) with $\partial/\partial\rho$ as their generator.

2.1.2. Wave equation

The covariant d'Alembertian or wave equation associated with the diagonal line-element (5) is the following:

$$\left(1 - \frac{1}{\rho}\right)^{-1}\frac{\partial^2\psi}{\partial\tau^2} - \frac{1}{\rho^2}\frac{\partial}{\partial\rho}\left[\rho^2\left(1 - \frac{1}{\rho}\right)\frac{\partial\psi}{\partial\rho}\right] - \frac{\Delta_{S^2}\psi}{\rho^2} = 0, \tag{8}$$

where Δ_{S^2} is the Laplace operator (with negative eigenvalues) belonging to the unit-radius round sphere S^2. Notice that we use ψ for the wave field associated with the static time coordinate τ (or associated with its counterpart T) introduced above, whereas in the introduction we have used U for the wave field. In the follow-up article [2] we use U for the wave field associated with a certain time variable t related to ingoing Eddington–Finkelstein coordinates. Our numerical work in [2] is based on t (which is why U and t, rather

than ψ and T, appear in the introduction), but we do not consider U or t again in this article. For flat spacetime T and t are the same, and so ψ and U are also formally the same for $\mathrm{m} = 0$.

Introducing the standard set $Y_{lm}(\theta, \phi)$ of basis functions for square-integrable functions on S^2, we consider an appropriate expansion

$$\psi(\tau, \rho, \theta, \phi) = \sum_{l,m} \psi_{lm}(\tau, \rho) Y_{lm}(\theta, \phi) \tag{9}$$

of the field ψ in terms of spherical-harmonic modes ψ_{lm}. The spherical-harmonic transform of (8),

$$\left(1 - \frac{1}{\rho}\right)^{-1} \frac{\partial^2 \psi_l}{\partial \tau^2} - \frac{1}{\rho^2} \frac{\partial}{\partial \rho} \left[\rho^2 \left(1 - \frac{1}{\rho}\right) \frac{\partial \psi_l}{\partial \rho}\right] + \frac{l(l+1)\psi_l}{\rho^2} = 0, \tag{10}$$

is the PDE governing the evolution of a generic mode ψ_l. On ψ_l we have suppressed the m, since it does not appear in the PDE.

Addition of a single simple term to (10) yields a modified wave equation flexible enough to describe either the mode evolution of an electromagnetic field A_β or the mode evolution of small gravitational perturbations $\delta g_{\alpha\beta}$ on the Schwarzschild background. The modified equation is

$$\left(1 - \frac{1}{\rho}\right)^{-1} \frac{\partial^2 \psi_l}{\partial \tau^2} - \frac{1}{\rho^2} \frac{\partial}{\partial \rho} \left[\rho^2 \left(1 - \frac{1}{\rho}\right) \frac{\partial \psi_l}{\partial \rho}\right] + \frac{l(l+1)\psi_l}{\rho^2} - \frac{\jmath^2 \psi_l}{\rho^3} = 0 \tag{11}$$

with the *spin* $\jmath = 0, 1, 2$ corresponding to scalar, electromagnetic, and gravitational radiation. We review the history of this correspondence in the next paragraph. We may cast (11) in a particularly simple form via simultaneous transformation of the independent and dependent variables. Indeed, setting $\Psi_l = \rho \psi_l$ and here viewing $\partial/\partial\rho_*$ as shorthand for $(1 - \rho^{-1})\partial/\partial\rho$, we rewrite (11) as follows:

$$\frac{\partial^2 \Psi_l}{\partial \tau^2} - \frac{\partial^2 \Psi_l}{\partial \rho_*^2} + V(\rho) \Psi_l = 0. \tag{12}$$

The *Regge–Wheeler potential*

$$V(\rho) = \left(1 - \frac{1}{\rho}\right) \left[\frac{l(l+1)}{\rho^2} + \frac{1 - \jmath^2}{\rho^3}\right] \tag{13}$$

would depend only implicitly on ρ_* where we using ρ_* as the independent variable. As we will see in Section 2.2.3, the Laplace transform of (12) is important theoretically, since it elucidates the role of Laplace frequency as a spectral parameter.

Wheeler derived the $j = 1$ version of (12,13) in 1955 [24], showing that each of the two polarization states for an electromagnetic field on the Schwarzschild geometry is described by one copy of the equation. Regge and Wheeler [25] then derived the $\jmath = 2$ equation for odd-parity (or axially) gravitational perturbations in 1957, and Zerilli introduced a similar equation describing even-parity (or polar) gravitational perturbations in 1970 [26]. In the 1970s Chandrasekhar and Detweiler demonstrated that the Zerilli equation can be derived from (12), although the derivation involves differential operations (see [27] and references therein).

Adopting μ as the time coordinate, we define $\varphi_l(\mu, \rho) = \psi_l(\mu + \rho_*, \rho)$ and write (11) as

$$2 \frac{\partial^2 \varphi_l}{\partial \mu \partial \rho} + \frac{2}{\rho} \frac{\partial \varphi_l}{\partial \mu} - \frac{1}{\rho^2} \frac{\partial}{\partial \rho} \left[\rho^2 \left(1 - \frac{1}{\rho}\right) \frac{\partial \varphi_l}{\partial \rho}\right] + \frac{l(l+1)\varphi_l}{\rho^2} - \frac{\jmath^2 \varphi_l}{\rho^3} = 0. \tag{14}$$

Another way to obtain this wave equation is to form the d'Alembertian associated with (7) and then implement a spherical-harmonic transformation. Similar to above, we may either set $\Phi_l = \rho \varphi_l$ or $\Phi_l(\mu, \rho) = \Psi_l(\mu + \rho_*, \rho)$, thereby expressing (12) as

Table 1
Wave fields and their relevance

Static time coordinate system (τ,ρ)		Retarded time coordinate system (μ,ρ)	
$\psi_l(\tau,\rho)$	ODE for L.t. is analogous to the spherical Bessel equation	$\varphi_l(\mu,\rho)$	$\jmath=0$ ODE for L.t. is directly the confluent Heun equation
$\Psi_l(\tau,\rho)$	ODE for L.t. elucidates role of σ as a spectral parameter	$\Phi_l(\mu,\rho)$	ODE for L.t. has outgoing solution normalized at ∞

L.t. stands for *Laplace transform*.
As we discuss in Section 2.2, via the Laplace transform we trade a PDE for an ODE.

$$2\frac{\partial^2\Phi_l}{\partial\mu\partial\rho_*}-\frac{\partial^2\Phi_l}{\partial\rho_*^2}+V(\rho)\Phi_l=0, \tag{15}$$

again viewing $\partial/\partial\rho_*$ as a shorthand. As we will see, for a given l the FDRK is built from the outgoing solution to the formal Laplace transform of (15). Table 1 lists the wave fields we have introduced, and it also briefly describes the theoretical importance of each field's Laplace transform. The statements made in the table are explained in Sections 2.2 and 2.3.

2.2. Laplace transform and radial wave equation

2.2.1. Laplace transform

The Schwarzschild geometry is static. [7] In turn, the variable coefficients of the linear wave equation described in the last subsection do not depend on τ, a scenario permitting study of the equation via the technique of Laplace transform [47]. Let $\mathscr{L}$ denote the transform operation,

$$\mathscr{L}[g](\sigma)=\int_0^\infty \mathrm{e}^{-\sigma\tau}g(\tau)\,\mathrm{d}\tau. \tag{16}$$

Here we use σ for the variable dual to τ with respect to the Laplace transform. We may define a physical variable $s=\sigma/(2\mathrm{m})$, with dimensions of inverse length, which is dual to t and satisfies $st=\sigma\tau$. We may also define a formal Laplace transformation on the retarded time μ by replacing τ with μ in the last equation. For the time being we proceed with the transformation on τ.

2.2.2. Laplace transform of the wave equation

Let us formally compute the Laplace transform of (11), in order to get an ODE in the radial variable ρ. We set $\hat{\psi}_l=\mathscr{L}[\psi_l]$ and assume that the initial data $\psi_l(0,\rho)$ and $\dot{\psi}_l(0,\rho)$ vanish in a neighborhood of ρ, as is true for compactly supported data so long as we choose ρ large enough. This assumption ensures formally that upon Laplace transformation we may replace τ partial differentiation by σ multiplication. Whence, after some simple algebra we find

$$\frac{\mathrm{d}^2\hat{\psi}_l}{\mathrm{d}\rho^2}+\frac{2\rho-1}{\rho(\rho-1)}\frac{\mathrm{d}\hat{\psi}_l}{\mathrm{d}\rho}+\left[\frac{-\sigma^2\rho^2}{(\rho-1)^2}-\frac{l(l+1)}{\rho(\rho-1)}+\frac{\jmath^2}{\rho^2(\rho-1)}\right]\hat{\psi}_l=0 \tag{17}$$

for the Laplace transform of (11).

[7] More precisely, $\partial/\partial\tau$ is a hypersurface-orthogonal vector field which satisfies the Killing equation $\pounds_{\partial/\partial\tau}g_{\mu\nu}=0$, where $\pounds$ denotes Lie differentiation.

It is instructive to see what happens to (17) in the $\mathrm{m} \to 0^+$ limit. Before taking the limit, first recall that $\rho = (2\mathrm{m})^{-1} r$ and $\sigma = 2\mathrm{m}s$, so that the product $z = \sigma\rho = sr$ is independent of m. With this in mind, we divide the overall equation by a factor of σ^2 and find

$$\frac{\mathrm{d}^2\hat{\psi}_l}{\mathrm{d}z^2} + \frac{2z-\sigma}{z(z-\sigma)}\frac{\mathrm{d}\hat{\psi}_l}{\mathrm{d}z} + \left[\frac{-z^2}{(z-\sigma)^2} - \frac{l(l+1)}{z(z-\sigma)} + \frac{\sigma j^2}{z^2(z-\sigma)}\right]\hat{\psi}_l = 0, \tag{18}$$

where σ is now shorthand for 2 ms. Formally then, the $\mathrm{m} \to 0^+$ limit along with multiplication by z^2 sends the last equation into the *modified spherical Bessel equation* (MSBE) [40]:

$$z^2\frac{\mathrm{d}^2\hat{\psi}_l}{\mathrm{d}z^2} + 2z\frac{\mathrm{d}\hat{\psi}_l}{\mathrm{d}z} - \left[z^2 + l(l+1)\right]\hat{\psi}_l = 0. \tag{19}$$

As linearly independent solutions of the MSBE we could take

$$k_l(z) = \sqrt{\frac{\pi}{2z}}K_{l+1/2}(z), \quad i_l(z) = \sqrt{\frac{\pi}{2z}}I_{l+1/2}(z), \tag{20}$$

where $K_{l+1/2}(z)$, MacDonald's function, and $I_{l+1/2}(z)$ are standard modified (cylindrical) Bessel functions of half-integer order [22].

2.2.3. Laplace frequency as a spectral parameter

We observe that

$$\frac{\mathrm{d}^2\hat{\Psi}_l}{\mathrm{d}\rho_*^2} - V(\rho)\hat{\Psi}_l = \sigma^2\hat{\Psi}_l \tag{21}$$

is the formal Laplace transform of (12). This is a remarkable form of the radial ODE for several reasons. First, we could consider it in the context of an eigenvalue problem, although one in which the operator on the LHS is not self-adjoint. More precisely, suppose we seek solutions to (21) which vanish at $\rho = \rho_\mathrm{B}$ (a fixed constant) and are also asymptotically outgoing, that is behave as $\mathrm{e}^{-\sigma\rho}$ for large ρ. We do then (numerically) find solutions corresponding to a discrete (but finite) set of σ values, but these values lie in the lefthalf plane. [8] For such σ the term $\mathrm{e}^{-\sigma\rho}$ blows up as ρ gets large, spoiling any possible self-adjointness for $\mathrm{d}^2/\mathrm{d}\rho_*^2 - V(\rho)$ on $[\rho_\mathrm{B}, \infty)$ with these boundary conditions.

Let us also consider the Bessel analog of (21). Namely,

$$\frac{\mathrm{d}^2\hat{\Psi}_l}{\mathrm{d}\rho^2} - \frac{l(l+1)}{\rho^2}\hat{\Psi}_l = \sigma^2\hat{\Psi}_l. \tag{22}$$

We reach this equation by passing to $z = \sigma\rho$ as above, taking the $\mathrm{m} \to 0^+$ limit, and then passing back to $\rho = z/\sigma$. For the type of eigenvalue problem mentioned above, the operator $\mathrm{d}^2/\mathrm{d}\rho^2 - l(l+1)/\rho^2$ is also not self-adjoint, but this fact is not our prime concern now. The discussion in Section 2.2.2 shows that (22) has solutions, such as $(\sigma\rho)^{1/2}K_{l+1/2}(\sigma\rho)$, of a special form. Indeed, they simultaneously solve an ODE in the spectral parameter σ [48]

$$\frac{\mathrm{d}^2\hat{\Psi}_l}{\mathrm{d}\sigma^2} - \frac{l(l+1)}{\sigma^2}\hat{\Psi}_l = \rho^2\hat{\Psi}_l. \tag{23}$$

[8] The results of subsequent sections justify this statement, although in what follows we work with a different form of the ODE stemming from yet another transformation $\hat{\Psi}_l = \exp(-\sigma\rho_*)\hat{\Phi}_l$ of the dependent variable. See Section 2.3.2 and what follows.

Accordingly, we describe solutions to (22) as *bispectral*. Solutions to the more complicated ODE (21) are not bispectral in this sense, and the lack of an associated differential equation in the parameter σ complicates our numerical investigations. More comments on this point follow in Section 3.1.2.

2.3. Normal and normalized form of the radial wave equation

2.3.1. Normal form

Standard analysis [49,50] of the ODE (17) shows that $\rho = 0$ and $\rho = 1$ are regular singular points, corresponding respectively to indicial exponents $\pm\jmath$ and $\pm\sigma$, whereas $\rho = \infty$ is an irregular singular point [50]. To put (17) in a "normal form", we transform the dependent variable $\hat{\psi}_l$ in order to (i) set one indicial exponent to zero at each singular point and (ii) "peel-off" the essential singularity at infinity as best we can. To this end, let us set

$$\hat{\psi}_l = \rho^{\jmath}(\rho-1)^{-\sigma}\mathrm{e}^{-\sigma\rho}\Theta_l = \rho^{\jmath}\mathrm{e}^{-\sigma\rho_*}\Theta_l. \tag{24}$$

Our choice of peeling off $\exp(-\sigma\rho)$ indicates our intention to examine asymptotically outgoing radiation fields. We have peeled off a factor of $(\rho-1)^{-\sigma}$ rather than $(\rho-1)^{\sigma}$ in order that the tortoise coordinate appears in the argument of the exponential factor in the transformation. Eq. (17) then becomes

$$\frac{\mathrm{d}^2\Theta_l}{\mathrm{d}\rho^2} + \left[-2\sigma + \frac{1+2\jmath}{\rho} + \frac{1-2\sigma}{\rho-1}\right]\frac{\mathrm{d}\Theta_l}{\mathrm{d}\rho} + \left[\frac{-2\sigma(1+\jmath)}{\rho-1} + \frac{\jmath(\jmath+1)-l(l+1)}{\rho(\rho-1)}\right]\Theta_l = 0. \tag{25}$$

We remark that one may also obtain the $\jmath = 0$ version of (25) directly from (14) via formal Laplace transform on the retarded time μ, i. e. for $\jmath = 0$ we can say $\Theta_l = \hat{\varphi}_l$.

Eq. (25) is a realization of the (*singly*) *confluent Heun equation* [41,42]

$$\frac{\mathrm{d}^2G}{\mathrm{d}\rho^2} + \left[\beta + \frac{\gamma}{\rho} + \frac{\delta}{\rho-1}\right]\frac{\mathrm{d}G}{\mathrm{d}\rho} + \left[\frac{\alpha\beta}{\rho-1} + \frac{q}{\rho(\rho-1)}\right]G = 0, \tag{26}$$

which has the generalized Riemann scheme [42]

$$\begin{bmatrix} 1 & 1 & 2 & \\ 0 & 1 & \infty & ;\rho \\ 0 & 0 & \alpha & ;q \\ 1-\gamma & 1-\delta & \gamma+\delta-\alpha & \\ & & 0 & \\ & & -\beta & \end{bmatrix}. \tag{27}$$

The first three columns of the scheme's second row indicate singular-point locations, while the corresponding columns of the first row indicate their types. That is to say, $\rho = 0$ and $\rho = 1$ are regular singular points and ∞ is an irregular singular point which arises as the confluence of *two* regular singular points (the 2 in the third column indicates this confluence). Appendix B of [1] shows how the confluent Heun equation arises from the *Heun equation*, an ODE similar to the hypergeometric equation, although possessing four rather than three regular singular points. The remaining information in the first two columns specifies the indicial exponents at the regular singular points, while that in the third column specifies the Thomé exponents corresponding to the two *normal solutions* about the point at ∞. These solutions have the asymptotic behavior

$$G^{+} \sim \rho^{-\alpha}\mathrm{e}^{0\cdot\rho}, \quad G^{-} \sim \rho^{-\gamma-\delta+\alpha}\mathrm{e}^{-\beta\rho}, \tag{28}$$

as $\rho \to \infty$ (in some sector which we discuss later). Finally, in the fourth column we have the independent variable ρ as well as the *accessory parameter* q. An ODE with the singularity structure of the confluent Heun equation is determined by the indicial exponents belonging to the regular singularities along with the Thomé exponents only up to a free parameter q. See Appendix B of [1] for details.

2.3.2. Normalized form at infinity

Viewed as the confluent Heun equation, we see that our radial wave equation (25) has the following generalized Riemann scheme:

$$\begin{bmatrix} 1 & 1 & 2 & & \\ 0 & 1 & \infty & & ;\rho \\ 0 & 0 & 1+\jmath & ;\jmath(\jmath+1)-l(l+1) & \\ -2\jmath & 2\sigma & 1+\jmath-2\sigma & & \\ & & 0 & & \\ & & 2\sigma & & \end{bmatrix}, \tag{29}$$

showing that the normal solutions to (25) obey

$$\Theta_l^+ \sim \rho^{-1-\jmath} e^{0\cdot\rho}, \quad \Theta_l^- \sim \rho^{-1-\jmath+2\sigma} e^{2\sigma\rho}, \tag{30}$$

as $\rho \to \infty$. We may also write $\Theta_l^- \sim \rho^{-1-\jmath}\exp(2\sigma\rho_*)$ for the large-ρ behavior of the second solution. The scheme (27) shows that confluent Heun functions are generally specified by five parameters. However, our specific scheme (29) corresponds to a two-parameter family of functions (those parameters being σ and l, with $\jmath$ viewed as fixed). This is comparable to the situation regarding the flatspace radial wave equation and the associated one-parameter family of Bessel functions (that parameter being the Bessel order $l+1/2$). Bessel functions (suitably transformed) are a one-parameter family within the larger two-parameter class of confluent hypergeometric functions (which may also be represented as either Whittaker functions or Coulomb wave functions) [51–53].

Numerical considerations below dictate that we work instead with an outgoing solution which is "normalized at infinity", that is to say approaches unity for large ρ. Therefore, we now enact the transformation $\Theta_l = \rho^{-1-\jmath}\hat{\Phi}_l$, or in terms of the original field $\hat{\psi}_l = \rho^{-1}\exp(-\sigma\rho_*)\hat{\Phi}_l$, whereupon we find

$$\frac{d^2\hat{\Phi}_l}{d\rho^2} + \left[-2\sigma - \frac{1}{\rho} + \frac{1-2\sigma}{\rho-1}\right]\frac{d\hat{\Phi}_l}{d\rho} + \left[\frac{1-\jmath^2}{\rho^2} - \frac{1-\jmath^2+l(l+1)}{\rho(\rho-1)}\right]\hat{\Phi}_l = 0 \tag{31}$$

as the ODE satisfied by $\hat{\Phi}_l$. Remarkably, this equation agrees with that obtained directly from (15) via formal Laplace transform on the retarded time μ, whence our choice $\hat{\Phi}_l$ with a hat for the dependent variable here. We emphasize that this statement is true for all possible spin values ($\jmath = 0, 1, 2$), whereas the identification $\Theta_l = \hat{\varphi}_l$ mentioned before is valid only for $j = 0$.

We again set $z = \sigma\rho = sr$ (independent of m) and divide (31) by an overall factor of σ^2, thereby reaching the following particularly useful form of the radial wave equation:

$$\frac{d^2\hat{\Phi}_l}{dz^2} + \left[-2 - \frac{1}{z} + \frac{1-2\sigma}{z-\sigma}\right]\frac{d\hat{\Phi}_l}{dz} + \left[\frac{1-\jmath^2}{z^2} - \frac{1-\jmath^2+l(l+1)}{z(z-\sigma)}\right]\hat{\Phi}_l = 0. \tag{32}$$

With $W_l(z;\sigma)$ and $Z_l(z;\sigma)$ respectively denoting the outgoing and ingoing solutions to this ODE, the corresponding solutions to (31) are $W_l(\sigma\rho;\sigma)$ and $Z_l(\sigma\rho;\sigma)$ with σ here viewed as fixed. As $\rho \to \infty$ these obey

$$W_l(\sigma\rho;\sigma) \sim 1, \quad Z_l(\sigma\rho;\sigma) \sim e^{2\sigma\rho_*}. \tag{33}$$

Respectively, we might also denote W_l and Z_l by $\hat{\Phi}_l^+$ and $\hat{\Phi}_l^-$.

Recall that $\sigma \to 0$ as $\mathrm{m} \to 0^+$, whereas the product $z = \sigma\rho$ remains fixed in the said limit. Therefore, in the $\mathrm{m} \to 0^+$ limit Eq. (32) becomes an ODE

$$\frac{\mathrm{d}^2\hat{\Phi}_l}{\mathrm{d}z^2} - 2\frac{\mathrm{d}\hat{\Phi}_l}{\mathrm{d}z} - \frac{l(l+1)}{z^2}\hat{\Phi}_l = 0 \tag{34}$$

which could also be obtained straight from the MSBE (19) via the transformation $\hat{\psi}_l = z^{-1}\mathrm{e}^{-z}\hat{\Phi}_l$. In terms of the two-parameter functions introduced above, $W_l(z;0)$ and $Z_l(z;0)$ are respectively the formal outgoing and ingoing solutions to (34). We shall also write these as simply $W_l(z)$ and $Z_l(z)$ when there is no cause for confusion. A few examples may be illuminating. The first three outgoing solutions to the MSBE are the following *spherical MacDonald functions*:

$$k_0(z) = \frac{\mathrm{e}^{-z}}{z}, \quad k_1(z) = \frac{\mathrm{e}^{-z}}{z}\left(1 + \frac{1}{z}\right), \quad k_2(z) = \frac{\mathrm{e}^{-z}}{z}\left(1 + \frac{3}{z} + \frac{3}{z^2}\right). \tag{35}$$

Now consider the following polynomials in inverse z:

$$W_0(z) = 1, \quad W_1(z) = 1 + \frac{1}{z}, \quad W_2(z) = 1 + \frac{3}{z} + \frac{3}{z^2}. \tag{36}$$

From the discussion above we see that these are outgoing solutions to (34), and clearly ones which are normalized at infinity. We shall see that outgoing solutions $W_l(z;\sigma)$ to (32) are similar, albeit not simple polynomials in inverse $z = \sigma\rho$.

2.3.3. Asymptotic expansion for normalized form

For our purposes Eq. (32) will prove the most useful form of the frequency-space radial wave equation, so let us describe its outgoing solution $W_l(z;\sigma)$ as a formal asymptotic series. Our discussion in Section 2.3.2 focused on the variable ρ, but the same normalization issues are pertinent for z. First, for convenience we set $\kappa = 1 - \jmath^2$; hence κ takes the values $1, 0, -3$ for scalar, electromagnetic, and gravitational cases, respectively.

Assume a solution to (32) taking the form

$$W_l(z;\sigma) \sim \sum_{n=0}^{\infty} d_n(\sigma) z^{-n}, \tag{37}$$

demanding that $d_0(\sigma) = 1$. Of course the remaining $d_n(\sigma)$ will in general also depend on l and κ, but we suppress this dependence here. Standard calculations then determine both $d_1(\sigma) = l(l+1)/2$ and the following three-term recursion relation:

$$d_{n+1}(\sigma) = \frac{[l(l+1) - n(n+1)]d_n(\sigma) + \sigma(n^2 + \kappa - 1)d_{n-1}(\sigma)}{2(n+1)}. \tag{38}$$

A dominant balance argument shows the $d_{n+1}(\sigma)/d_n(\sigma) = \mathrm{O}(n)$, whence the series (37) is generally divergent and only summable in the sense of an asymptotic expansion. Olver shows that the sector of validity for this asymptotic expansion includes the entire z-plane (see Chapter 7 of [54]).

Set $c_n = d_n(0)$. Sending $\sigma \mapsto 0$ in (38) then yields the simple two-term recursion relation

$$c_{n+1} = \frac{[l(l+1) - n(n+1)]}{2(n+1)}\, c_n, \tag{39}$$

with solution (see [22, p. 202])

$$c_n = \frac{\Gamma(l+n+1)}{2^n n!\Gamma(l-n+1)}. \tag{40}$$

When l is a positive integer, as is the case here, the series $\sum_{n=0}^{\infty} c_n z^{-n}$ truncates, so the solution $W_l(z)$ is a polynomial of degree l in inverse z. All coefficients c_n are positive and nonzero, and we can ultimately conclude that all zeros of $W_l(z)$ lie in the lefthalf z-plane. Furthermore, the last nonzero coefficient is

$$c_l = \frac{\Gamma(2l+1)}{2^l l!}, \tag{41}$$

and from this formula we may appeal to the asymptotic behavior of the gamma function (see [40, p. 486]) in order to show

$$c_l \sim \Gamma(l) 2^l \sqrt{l/\pi} \tag{42}$$

as l becomes large.

2.4. Radiation outer boundary conditions

This section derives and discusses ROBC for a single spherical-harmonic mode $\psi_{lm}(\tau,\rho)$, but we continue the practice of everywhere suppressing the subscript m. This section's formulae are valid for all possible spin values $\jmath = 0, 1, 2$; however, for concrete examples we choose $\jmath = 0$.

2.4.1. Derivation of the radiation kernel

Although we will now derive exact equations, let us define the radial computational domain to be (the product of 2m and) the ρ interval $[1, \rho_{\mathrm{B}}]$. The radial numerical mesh will be a discretization of this interval. Now consider an infinite radial domain S defined by $\rho > \rho_{\max}$, with $\rho_{\max} < \rho_{\mathrm{B}}$. Let S_0 denote the intersection of $\mathsf{S} \times [0,\infty)$ with an initial $\tau = 0$ Cauchy surface. Assume that the initial data $\psi_l(0,\rho)$ and $\dot{\psi}_l(0,\rho)$ are of compact support and, moreover, vanish on S_0. The condition $\rho_{\max} < \rho_{\mathrm{B}}$ ensures that the domain edge ρ_{B} does not intersect the support of the initial data (see Fig. 2). Then the analysis of the last section establishes the formal expression

$$\psi_l(\tau,\rho) = \mathscr{L}^{-1}\left[a_l(\sigma)\frac{\mathrm{e}^{-\sigma\rho_*} W_l(\sigma\rho;\sigma)}{\rho} + b_l(\sigma)\frac{\mathrm{e}^{-\sigma\rho_*} Z_l(\sigma\rho;\sigma)}{\rho}\right](\tau) \tag{43}$$

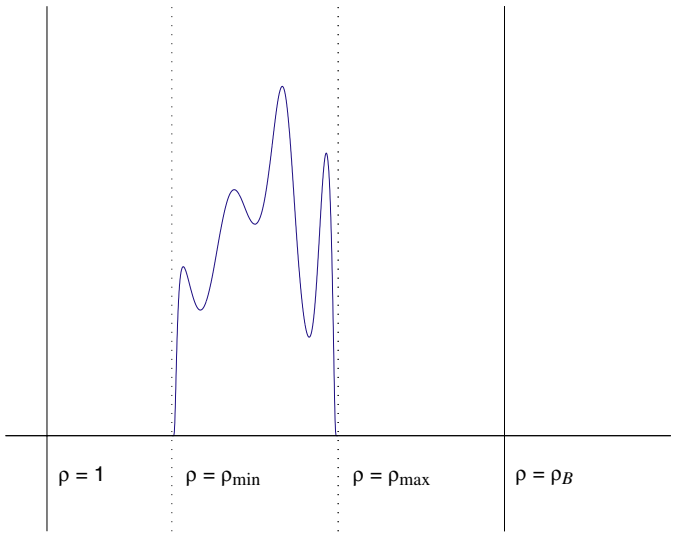

Fig. 2. Initial wave-packet configuration in the frequency domain. The undulations represent the initial data which is compactly supported on $[\rho_{\min}, \rho_{\max}]$. The domain $\mathsf{S}_0 = (\rho_{\max}, \infty)$ lies to the right of the data.

as the general solution to the wave equation (11) on the history $\mathsf{S} \times [0, \infty)$ of S_0. Here the coefficients $a_l(\sigma)$ and $b_l(\sigma)$ are arbitrary functions analytic in the righthalf σ-plane. Now, $Z_l(\sigma\rho;\sigma) \sim \exp(2\sigma\rho_*)$ as $\rho \to \infty$, showing that $b_l(\sigma)$ must be zero (for otherwise the solution is not asymptotically outgoing as expected for an initial "wave packet" of compact support).

The solution within the computational domain is also obtained as above via inverse Laplace transform. However, now the relevant frequency-space radial function solves the inhomogeneous version of (17), in which case the source

$$(\rho^2 - \rho)^{-1} J_l(\rho;\sigma) = -\rho^2(\rho-1)^{-2}\left[\dot{\psi}_l(0,\rho) + \sigma\psi_l(0,\rho)\right] \tag{44}$$

replaces zero on the RHS of the equation, as is necessary for non-trivial initial data. This solution appropriately matches $a_l(\sigma)\rho^{-1}\mathrm{e}^{-\sigma\rho_*}W_l(\sigma\rho;\sigma)$ at the largest radius $\rho_{\max}$ on which the data are supported. Let us further assume that the initial data are supported only on $[\rho_{\min}, \rho_{\max}]$, where $\rho_{\min} > 1$ (again, see Fig. 2). In this case, taking the second solution $\rho^{-1}\exp(-\sigma\rho_*)Z_l(\sigma\rho;\sigma)$ as ingoing at the horizon and using well-known methods associated with one-dimensional Green's functions, one can show that

$$a_l(\sigma) \propto \int_{\rho_{\min}}^{\rho_{\max}} \exp(-\sigma\rho)(\rho-1)^{-\sigma}\rho^{-1}Z_l(\sigma\rho;\sigma)J_l(\rho;\sigma)\,\mathrm{d}\rho, \tag{45}$$

where the proportionality constant is determined by calculating the Wronskian of the two chosen linearly independent solutions to the homogeneous equation [50].

Let us now derive the explicit form of the radiation kernel, assuming that we now work in the region $\rho > \rho_{\mathrm{B}}$. Consistent with our presentation thus far, we denote by $\psi_l(\tau,\rho)$ the function satisfying

$$\mathscr{L}[\psi_l](\sigma,\rho) = \hat{\psi}_l(\sigma,\rho) = a_l(\sigma)\rho^{-1}\mathrm{e}^{-\sigma\rho_*}W_l(\sigma\rho;\sigma). \tag{46}$$

Differentiation of this formula by ρ then gives

$$\partial_\rho\hat{\psi}_l(\sigma,\rho) = \left[\sigma\frac{W_l'(\sigma\rho;\sigma)}{W_l(\sigma\rho;\sigma)} - \sigma - \frac{\sigma}{\rho-1} - \frac{1}{\rho}\right]\hat{\psi}_l(\sigma,\rho), \tag{47}$$

with the prime denoting differentiation with respect to the first slot of $W_l(z;\sigma)$. Next, we rearrange terms and introduce some new symbols, thereby arriving at

$$\frac{\sigma\hat{\psi}_l(\sigma,\rho)}{\mathsf{N}(\rho)} + \frac{\partial_\rho\hat{\psi}_l(\sigma,\rho)}{\mathsf{M}(\rho)} + \frac{\hat{\psi}_l(\sigma,\rho)}{\mathsf{M}(\rho)\rho} = \rho^{-1}\mathsf{N}(\rho)\hat{\psi}_l(\sigma,\rho)\left[\sigma\rho\frac{W_l'(\sigma\rho;\sigma)}{W_l(\sigma\rho;\sigma)}\right], \tag{48}$$

where in terms of the function $F(\rho)$ appearing in the line-element (5) we have introduced the temporal lapse function $\mathsf{N}(\rho) = F^{1/2}(\rho)$ and the radial lapse function $\mathsf{M}(\rho) = F^{-1/2}(\rho)$. The metrical function N describes the proper-time separation between neighboring three-dimensional level-τ hypersurfaces, whereas, in a given such three-surface, M describes the proper-radial separation between neighboring concentric two-spheres [28]. Inverse Laplace transformation of the last equation yields

$$\frac{1}{\mathsf{N}}\frac{\partial\psi_l}{\partial\tau} + \frac{1}{\mathsf{M}}\frac{\partial\psi_l}{\partial\rho} + \frac{\psi_l}{\mathsf{M}\rho} = \rho^{-1}\mathsf{N}(\rho)\psi_l(\tau,\rho) \;*\; \mathscr{L}^{-1}\left[\sigma\rho_{\mathrm{B}}\frac{W_l'(\sigma\rho_{\mathrm{B}};\sigma)}{W_l(\sigma\rho_{\mathrm{B}};\sigma)}\right](\tau), \tag{49}$$

with $*$ here indicating Laplace convolution (defined just below). On this equation we remark that the direction $\mathsf{N}^{-1}\partial/\partial\tau + \mathsf{M}^{-1}\partial/\partial\rho$ is null and outgoing, whence the derivative of the field appearing on the LHS is along a characteristic. The last equation holds in particular at ρ_{B}, and as our ROBC we adopt the following:

$$\left[\frac{1}{\mathsf{N}}\frac{\partial\psi_l}{\partial\tau}+\frac{1}{\mathsf{M}}\frac{\partial\psi_l}{\partial\rho}+\frac{\psi_l}{\mathsf{M}\rho}\right]\Bigg|_{\rho=\rho_{\mathrm{B}}}=\rho_{\mathrm{B}}^{-1}\mathsf{N}(\rho_{\mathrm{B}})\int_0^\tau \omega_l(\tau-\tau';\rho_{\mathrm{B}})\psi_l(\tau',\rho_{\mathrm{B}})\,\mathrm{d}\tau', \tag{50}$$

where we have introduced the *time-domain radiation kernel* (TDRK)

$$\omega_l(\tau;\rho_{\mathrm{B}})=\mathscr{L}^{-1}\left[\sigma\rho_{\mathrm{B}}\frac{W_l'(\sigma\rho_{\mathrm{B}};\sigma)}{W_l(\sigma\rho_{\mathrm{B}};\sigma)}\right](\tau). \tag{51}$$

We refer to that appearing within the square brackets on the RHS as the *frequency-domain radiation kernel* (FDRK), and we also denote it by

$$\hat{\omega}_l(\sigma;\rho_{\mathrm{B}})=\sigma\rho_{\mathrm{B}}\frac{W_l'(\sigma\rho_{\mathrm{B}};\sigma)}{W_l(\sigma\rho_{\mathrm{B}};\sigma)}. \tag{52}$$

We assume that the FDRK $\hat{\omega}_l(\sigma;\rho_{\mathrm{B}})$ has the appropriate σ-decay necessary for a well-defined $\omega_l(\tau;\rho_{\mathrm{B}})=\mathscr{L}^{-1}[\hat{\omega}_l(\sigma;\rho_{\mathrm{B}})](\tau)$. Both $\omega_l(\tau;\rho_{\mathrm{B}})$ and $\hat{\omega}_l(\sigma;\rho_{\mathrm{B}})$ do of course depend on the values of l and ρ_{B} (and on the choice of spin $\jmath$), but to avoid clutter we will sometimes suppress this dependence and write simply $\omega(\tau)$ and $\hat{\omega}(\sigma)$. The ROBC could be written more simply in terms of $\Psi_l=\rho\psi_l$.

2.4.2. Representation of the kernel

In Section 4 we undertake a fairly thorough numerical investigation of the analytic behavior of both $W_l(\sigma\rho_{\mathrm{B}};\sigma)$ and $\hat{\omega}_l(\sigma;\rho_{\mathrm{B}})$ as functions of the complex variable σ. As a result of our investigation, we shall make the following conjectures regarding the FDRK $\hat{\omega}_l(\sigma;\rho_{\mathrm{B}})$. First, for l fixed $\hat{\omega}_l(\sigma;\rho_{\mathrm{B}})$ is analytic on $\mathbb{C}\setminus(-\infty,0]$, save for $N_l=N_l(\rho_{\mathrm{B}})\in\mathbb{Z}_{\geqslant 0}$ simple poles with locations $\{\sigma_{l,n}=\sigma_{l,n}(\rho_{\mathrm{B}}):n=1,\cdots,N_l\}$ lying in the lefthalf σ-plane. Second, $\hat{\omega}_l(\sigma;\rho_{\mathrm{B}})$ is bounded in a neighborhood of the origin $\sigma=0$. Third, $\mathrm{Re}\,\hat{\omega}_l(\sigma;\rho_{\mathrm{B}})$ is continuous and $\mathrm{Im}\,\hat{\omega}_l(\sigma;\rho_{\mathrm{B}})$ jumps by a sign across the branch cut along the negative $\mathrm{Re}\,\sigma$ axis. The integer $N_l(\rho_{\mathrm{B}})$ is constant over sizable regions of the ρ_{B} parameter space. However, the pole locations $\sigma_{l,n}$ do vary smoothly with respect to changes of ρ_{B}, apparently subject to

$$\sigma_{l,n}(\rho_{\mathrm{B}})\sim\sum_{k=1}^{\infty}\sigma_{l,n,k}\rho_{\mathrm{B}}^{-k}, \tag{53}$$

where the $\sigma_{l,n,k}$ are constants. This series is perhaps only summable as an asymptotic expansion, and we have only numerically observed the first two terms.

Let us now define the nth *pole strength* and a *cut profile* respectively via

$$\alpha_{l,n}(\rho_{\mathrm{B}})=-\rho_{\mathrm{B}}\sigma_{l,n}'(\rho_{\mathrm{B}}),\quad f_l(\chi;\rho_{\mathrm{B}})=\mathrm{Im}\;\hat{\omega}_l(\chi\mathrm{e}^{\mathrm{i}\pi};\rho_{\mathrm{B}}), \tag{54}$$

with $\chi\geqslant 0$ and the prime here standing for $\partial/\partial\rho_{\mathrm{B}}$ differentiation. Like the pole locations, both of these objects also vary with respect to changes of ρ_{B} as indicated. As can be inferred from the third conjecture of the last paragraph, it is the case that $\mathrm{Im}\;\hat{\omega}_l(\chi\mathrm{e}^{-\mathrm{i}\pi};\rho_{\mathrm{B}})=-f_l(\chi;\rho_{\mathrm{B}})$. To give a concrete example, we choose $\jmath=0$, $l=2$, and $\rho_{\mathrm{B}}=15$, in which case we have numerically found that $N_2(15)=2$, $\sigma_{2,n}(15)\simeq-0.0969\pm\mathrm{i}0.0612$, and $\alpha_{2,n}(15)\simeq-0.0936\pm\mathrm{i}0.0647$, for $n=1(+)$ and $2(-)$. For these parameter values the corresponding cut profile is shown in Fig. 3. The plot is typical in the sense that for all l and ρ_{B} considered here, $f_l(\chi;\rho_{\mathrm{B}})$ decays sharply in the $\chi\to 0^+$ and $\chi\to\infty$ limits (except for $l=0$ where the decay in the $\chi\to 0^+$ limit is not as sharp). However, the shape of the profile can be qualitatively different for other parameter values. Moreover, for certain exceptional values of the parameters, the profile can even blow up at a particular χ point, in which case numerical evidence suggests that the integral in (55) is defined in the sense of a Cauchy Principal Value. We discuss all of these issues in Section 4.1.

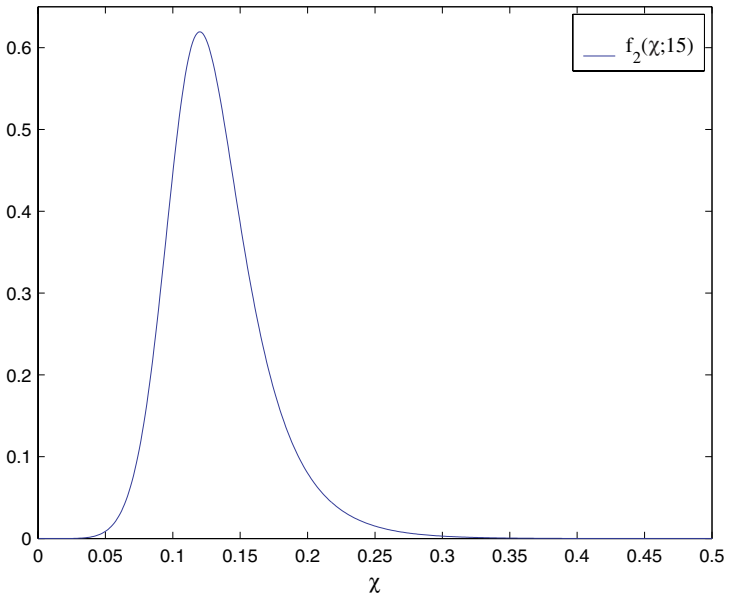

Fig. 3. Typical cut profile. For this plot $\jmath = 0$, $l = 2$, and $\rho_{\mathrm{B}} = 15$.

In terms of the pole locations and strengths and the cut profile, we claim that the FDRK has the representation (suppressing ρ_{B} dependence for now)

$$\hat{\omega}_l(\sigma) = \sum_{n=1}^{N_l} \frac{\alpha_{l,n}}{\sigma - \sigma_{l,n}} - \frac{1}{\pi} \int_0^\infty \frac{f_l(\chi)}{\sigma + \chi} \, \mathrm{d}\chi \tag{55}$$

for all σ not equal to a $\sigma_{l,n}$ and not lying on $(-\infty, 0]$. Despite the right closed bracket here, we shall also evaluate this representation at $\sigma = 0$. Given the described structure of the σ-function $\hat{\omega}_l(\sigma)$, the derivation of such a representation amounts to a simple exercise involving the Residue Theorem and a "keyhole" contour. Although we will often described the second term on the RHS of (55) as corresponding to a continuous set of poles, these are not really poles in the sense of complex analysis (which are properly isolated singularities). Formally, we compute the inverse Laplace transform of (55), with result

$$\omega_l(\tau) = \sum_{n=1}^{N_l} \alpha_{l,n} \exp(\sigma_{l,n}\tau) - \frac{1}{\pi} \int_0^\infty f_l(\chi) \exp(-\chi\tau) \, \mathrm{d}\chi. \tag{56}$$

Evidently then, direct numerical construction of the FDRK would amount to numerical computation of the pole locations and strengths and the cut profile. For $l \leqslant 10$ we consider such a direct construction in Section 4.2.

Section 1.2 of [2] shows how this brute-force approach may be bypassed insofar as implementation of ROBC is concerned. The basic idea is to approximate the FDRK (55) by a proper rational function,

$$\hat{\xi}_l(\sigma) = \sum_{n=1}^{d} \frac{\gamma_{l,n}}{\sigma - \beta_{l,n}}, \tag{57}$$

itself a sum of d discrete poles. Here we have suppressed the ρ_{B} dependence of the rational function $\hat{\xi}_l(\sigma)$ as well as that of the approximate pole strengths $\gamma_{l,n}$ and locations $\beta_{l,n}$. The approximation is tailored to have relative supremum error ε along the axis of imaginary Laplace frequency, that is

$$\sup_{y\in\mathbb{R}} \frac{\left|\hat{\xi}_l(\mathrm{i}y) - \hat{\omega}_l(\mathrm{i}y)\right|}{\left|\hat{\omega}_l(\mathrm{i}y)\right|} < \varepsilon. \tag{58}$$

As shown in [1,2,19,55], when using the inverse Laplace transform $\xi_l(\tau)$ of $\hat{\xi}_l(\sigma)$ as an approximate TDRK, ε also turns out to be a relevant error measure in the time domain. It proves far more efficient, given a fixed choice of accuracy ε, to base an implementation of ROBC on (57) rather than (a discretization of) the actual representation (55). The *kernel compression algorithm* [which produces the numbers $\gamma_{l,n}$ and $\beta_{l,n}$ appearing in (57)] is sketched in [19] and, in more detail, in [1,2,55].

2.4.3. Comparison with the Green's function method

Any temptation to identify the pole locations $\sigma_{l,n}(\rho_{\mathrm{B}})$ in the representation (55) with so-called quasinormal modes [56] should be resisted. For a given l there are an infinite number of quasinormal modes [56], fixed numerical values intrinsic to the blackhole geometry and certainly insensitive to any particular choice of outer boundary radius ρ_{B}. However, for $\rho_{\mathrm{B}} > 1$ the poles now under examination, that is the zeros in σ of the Heun-type function $W_l(\sigma\rho_{\mathrm{B}};\sigma)$, are finite in number, and they do depend on ρ_{B}. Moreover, the boundary value problem associated with these Heun zeros is different than the usual one associated with quasinormal modes. This usual boundary value problem was considered in the pioneering work [38] of Leaver, and more recently in a careful study by Andersson [39]. The goal of both authors was to examine a given multipole field $\psi_l(\tau,\rho) = \rho^{-1}\Psi_l(\tau,\rho)$ in terms of a Green's function representation involving initial data. Andersson refers to this as the initial value problem for the scalar field (or, more generally, for electromagnetic or gravitational perturbations), although when we mentioned that name in the first paragraph of the introduction we did not have this Green's function approach in mind. In Eq. (6) of [39], Andersson expresses the scalar field as

$$\Psi_l(\tau,\rho_*) = \int G_l(\rho_*,\rho'_*;\tau)\partial_\tau\Psi_l(0,\rho_*)\,\mathrm{d}\rho'_* + \int \partial_\tau G_l(\rho_*,\rho'_*;\tau)\Psi_l(0,\rho_*)\,\mathrm{d}\rho'_*. \tag{59}$$

In this equation we view the field Ψ_l introduced in (32) as depending on ρ_* (as Andersson does), and we have also slightly modified Andersson's notations to suit our own. The appropriate limits of ρ_* integration in (59) are discussed in [39]. This problem perhaps resembles our own; however, as we now demonstrate, it is different both in concept and detail.

Both Leaver and Andersson considered the (here Laplace) transform of the Green's function in (59), a frequency-domain Green's function $\hat{G}_l(\rho_*,\rho'_*;\sigma)$ associated with the following boundary value problem. The solution is pure ingoing at the horizon [$\hat{\Psi}^-_l(\sigma,\rho_*) \sim \exp(\sigma\rho_*)$ as $\rho_* \to -\infty$] and outgoing at infinity [$\hat{\Psi}^+_l(\sigma,\rho_*) \sim \exp(-\sigma\rho_*)$ as $\rho_* \to \infty$]. In fact, we briefly considered $\hat{G}_l(\rho_*,\rho'_*;\sigma)$ in and around (45), although we shall make no further use of it in this article or the follow-up article. Leaver and Andersson's approach was essentially to examine the value $\Psi_l(\tau,\rho_*)$, as expressed by (59), via a careful analysis of $\hat{G}_l(\rho_*,\rho'_*;\sigma)$. (Of no concern here, Leaver further considered more general driving source terms beyond just the initial data.) When $\hat{G}_l(\rho_*,\rho'_*;\sigma)$ is considered as an analytic function of complex σ and continued into the lefthalf plane, its pole locations are the quasinormal modes and there is also an associated branch cut along the negative $\mathrm{Re}\,\sigma$ axis [38,39,57]. These complex analytic features play a prominent role in describing the physical behavior of the field (see [38,39] and references therein).

Our key representation (55) stems from continuation into the lefthalf σ-plane of the FDRK $\hat{\omega}_l(\sigma;\rho_{\mathrm{B}})$, the expression (52) involving the logarithmic derivative of $W_l(\sigma\rho;\sigma) = \exp(\sigma\rho_*)\hat{\Psi}^+_l(\sigma,\rho)$. Here we again

view $\hat{\Psi}_l$ as depending on ρ_* rather than ρ_* as in the last paragraph. We stress that the FDRK $\hat{\omega}_l(\sigma;\rho_B)$ is not the Green's function $\hat{G}_l(\rho_*,\rho'_*;\sigma)$ considered by both Leaver and Andersson. Indeed, $\hat{\omega}_l(\sigma;\rho_B)$ is a *boundary* integral kernel. Moreover, it is built solely with the outgoing solution $\hat{\Psi}_l^+$ to the homogeneous ODE, whereas construction of the Green's function requires two linearly independent homogeneous solutions, $\hat{\Psi}_l^-$ and $\hat{\Psi}_l^+$. As mentioned, the pole locations associated with $\hat{\omega}_l(\sigma;\rho_B)$ are not the quasinormal modes, rather the special frequencies, finite in number, for which the outgoing solution $W_l(\sigma\rho;\sigma)$ also vanishes at ρ_B. Despite the fact that $\hat{G}_l(\rho_*,\rho'_*;\sigma)$ and $\hat{\omega}_l(\sigma;\rho_B)$ are different integral kernels, we remark that they share the same *qualitative* features in the lefthalf σ-plane (each has poles and a branch cut).

On top of these technical differences between our work and those of Leaver and Andersson, we point out that our overall goal is very different. As mentioned, their goal was to examine the actual value of the field via the representation (59) based on *spatial* convolution. On the contrary, our *boundary* kernel $\omega_l(\tau;\rho_B)$ is associated with *temporal* convolution, with the goal being to impose exact radiation boundary conditions at a given outer sphere B. That is to say, our goal is domain reduction via the introduction of integral convolution over the history ${}^3B$ of the boundary B. With this distinction in mind, compare our key Eq. (50) with Andersson's key equation, as we have written it in (59). Perhaps the approach of Andersson and Leaver could also be used to numerically implement exact radiation boundary conditions in an alternative way [by setting $\rho_* = \rho_B + \log(\rho_B - 1)$ in (59)], but they did not address this question *per se*. Moreover, such an approach would necessarily relate ROBC to the details of the data on the initial surface, which would seem awkward from a numerical standpoint. [9] Even were such an implementation carried out, memory and speed issues would inevitably arise. Besides developing exact ROBC via domain reduction, we also intend to provide an efficient and rapid implementation of these conditions. Although we do not do so until the sequel article, we develop the numerical methods in this article with these goals in mind.

3. Numerical evaluation of the outgoing solution and kernel

This section describes the handful of numerical methods used in this work. The first subsection describes a numerical method for evaluating the outgoing solution $W_l(\sigma\rho_B;\sigma)$ at a given complex σ, and this method allows us to numerically study the analytic structure of $W_l(\sigma\rho_B;\sigma)$ as a function of Laplace frequency. The lefthalf σ-plane is the domain of interest, and a study of $W_l(\sigma\rho_B;\sigma)$ on this domain, carried out in Section 4.1, justifies the key representation (55). As we have mentioned at the end of Section 2.4.2, in the follow-up article [2] we will consider numerical rational approximations to the FDRK $\hat{\omega}_l(\sigma;\rho_B)$ which are tailored to have small relative supremum error along the $\mathrm{Im}\,\sigma$ axis. Such an approximation (57) is a compressed kernel, and the crucial point is the following: *the algorithm for compressing kernels takes as input accurate numerical profiles for* $\mathrm{Re}\,\hat{\omega}_l(\mathrm{i}y;\rho_B)$ *and* $\mathrm{Im}\,\hat{\omega}_l(\mathrm{i}y;\rho_B)$ *where* $y \in \mathbb{R}$. Therefore, insofar as implementation of ROBC is concerned, we require numerical methods for obtaining these accurate numerical profiles. Section 3.2 describes two such methods. Although ultimately for use in the kernel compression algorithm found in the follow-up article [2], in Section 4.2.2 these methods will also help check the representation (55).

Before describing our numerical methods, we note that Leaver has analytically represented a solution to the Regge–Wheeler equation (more generally to the generalized spheroidal wave equation) as an infinite series in Coulomb wave functions, where the expansion coefficients obey a three-term recursion relation [44]. Such a series can alternatively be viewed as a sum of confluent hypergeometric functions. One approach towards our goal of numerically evaluating the outgoing solution would be to use the appropriate Leaver series. However, beyond the issue of numerically solving the relevant three-term recursion relation,

[9] We are definitely not critical of the most excellent works of Leaver and Andersson. Indeed, just as their Green's function technique would seem not the best way to implement ROBC, we do not believe we could directly reproduce their results with our boundary kernel technique.

numerical evaluation of Coloumb wave functions (for complex arguments) is already somewhat tricky [53]. Here we describe far simpler methods, which are nevertheless extremely accurate. Although simple, our methods are very accurate only for a limited range of frequencies (which happen to be precisely the frequencies we are interested in). The Leaver series is valid over the whole frequency plane. Although we have not compared our methods with the Leaver series, we believe they are better suited for our purposes.

3.1. Numerical evaluation of the outgoing solution

From now on let us simply refer to $W_l(\sigma\rho_{\mathrm{B}};\sigma)$ as a Heun function and $W_l(\sigma\rho_{\mathrm{B}})$ as a Bessel function. This is not quite correct since, as discussed in Section 2.3.2, $W_l(\sigma\rho_{\mathrm{B}};\sigma)$ and $W_l(\sigma\rho_{\mathrm{B}})$ respectively differ from Heun and Bessel functions by transformations on the dependent variable; however, this terminology will streamline our presentation. We now present numerical methods for computing the complex value $W_l(\sigma\rho_{\mathrm{B}};\sigma)$. The methods have been designed to successfully compute the similar value $W_l(\sigma\rho_{\mathrm{B}})$, formally $W_l(\sigma\rho_{\mathrm{B}};0)$ in our notation. $W_l(\sigma\rho)$ solves the ODE

$$\frac{\mathrm{d}^2\hat{\Phi}_l}{\mathrm{d}\rho^2} - 2\sigma\frac{\mathrm{d}\hat{\Phi}}{\mathrm{d}\rho} - \frac{l(l+1)}{\rho^2}\hat{\Phi} = 0 \tag{60}$$

obtained directly from (34) via the substitution $z = \sigma\rho$. Section 2.3.3 noted that $W_l(\sigma\rho)$ is a polynomial $\sum_{n=0}^{l} c_n(\sigma\rho)^{-n}$ of degree l in inverse $\sigma\rho$, with coefficients c_n given in (40). With the *exact* form of $W_l(\sigma\rho)$ we could in principle compute the value $W_l(\sigma\rho_{\mathrm{B}})$ directly. [10] Nevertheless, if we pretend that the exact form of $W_l(\sigma\rho)$ is not at our disposal, then the task of numerically computing $W_l(\sigma\rho_{\mathrm{B}})$ shares essential features with our ultimate task of computing $W_l(\sigma\rho_{\mathrm{B}};\sigma)$. The task of computing $W_l(\sigma\rho_{\mathrm{B}})$ has been an invaluable model, and for ease of presentation we mostly focus on it here.

3.1.1. Numerical integration

Focusing on the ρ-dependence of the solution, we write $W_l(\sigma\rho) = \sum_{n=0}^{l}(c_n\sigma^{-n})\rho^{-n}$. Since we shall not allow ourselves to evaluate $W_l(\sigma\rho_{\mathrm{B}})$ as $\sum_{n=0}^{l}(c_n\sigma^{-n})\rho_{\mathrm{B}}^{-n}$, we truncate the series after some fixed number $l-p$ of terms, assuming that

$$W_l(\sigma\rho) \sim \sum_{n=0}^{l-p}(c_n\sigma^{-n})\rho^{-n} \tag{61}$$

is at our disposal. Truncation by hand of this already finite series serves as a model for the scenario involving $W_l(\sigma\rho;\sigma)$, where only a divergent formal series, such as the one specified by (37) and (38), is at our disposal. With our truncated series we can still generate an accurate approximation to the value $W_l(\sigma\rho_\infty)$, so long as ρ_∞ is large enough. Let us set $\rho_\infty = \texttt{scale} * \rho_{\mathrm{B}}$, with `scale` a large number. Evaluation of the truncated sum and its ρ derivative at ρ_∞ then generates initial data for the ODE. Moreover, the generated data are approximate to the exact data $\{W_l(\sigma\rho_\infty), W_l^{\rho}(\sigma\rho_\infty)\}$ giving rise to $W_l(\sigma\rho)$. Here the superscript ρ denotes $\partial/\partial\rho$ differentiation, whereas a prime $'$ would denote differentiation in argument. We stress that our approximation to the exact data can be rendered arbitrarily accurate by choosing ρ_∞ large enough. Finally, we *numerically* integrate (60) in ρ from ρ_∞ to ρ_{B}, thereby computing a candidate for the value $W_l(\sigma\rho_{\mathrm{B}})$.

As it stands, the description in the last paragraph is an outline for a stable numerical method, provided $\mathrm{Re}\,\sigma > 0$. However, for the case $\mathrm{Re}\,\sigma < 0$ of interest the described method is not stable. To see why, consider the $l = 1$ outgoing solution $W_1(\sigma\rho) = 1 + (\sigma\rho)^{-1}$ to (60). As a second linearly independent solution to the $l = 1$ ODE, take the ingoing solution $Z_1(\sigma\rho) = \exp(2\sigma\rho)[1 - (\sigma\rho)^{-1}]$. Further, suppose that initial

[10] Due to the growth (42) of the Bessel coefficients, such direct computation is plagued by increasing loss of accuracy as l grows.

data for the ODE are obtained from a truncated sum as described above, with $\{1,0\}$ in place of exact data $\{1+(\sigma\rho_\infty)^{-1}, -\sigma(\sigma\rho_\infty)^{-2}\}$. The initial data $\{1,0\}$ correspond to a linear combination $aW_1(\sigma\rho)+bZ_1(\sigma\rho)$ with $a\simeq 1$ and b such that $bZ_1(\sigma\rho_\infty)\simeq 0$. To fix some realistic numbers, let $\rho_B=20$, $\texttt{scale}=250$ so $\rho_\infty=5000$, and $\sigma=-0.05$. Then we compute $a\simeq 1.0040$ and $bZ_1(\sigma\rho_\infty)\simeq 8.0320\times 10^{-6}$, where $b\simeq 1.1229\times 10^{212}$. The exact value we wish to calculate is $W_1(-1)=0$. However, with the chosen initial data, even an *exact* integration of (60) from $\rho_\infty=5000$ to $\rho_B=20$ yields the value 3.0393×10^{211}. Since error in the initial conditions is exponentially enhanced, the second solution $Z_1(-0.05\rho)$ dominates as ρ is decreased.

3.1.2. Two-component path integration

The simple discussion at hand suggests that we should complexify the variable ρ, rotating ρ_∞ off the real axis by an angle θ large enough to ensure that the product $\sigma\rho_\infty$ lies in the righthalf plane. Then integration along a ray in the complex ρ-plane from ρ_∞ towards the complex point $\exp(\mathrm{i}\theta)\rho_B$ (with ρ_B still real here) would exponentially *suppress* error in the initial conditions. At the end of such a ray integration, a second integration over an arc of θ radians would be needed to undo the phase of $\exp(\mathrm{i}\theta)\rho_B$. We effect such a rotation of the ρ coordinate as follows. We choose to work with the variable $z=\sigma\rho$, the solution $W_l(z)$, and the truncated series $\sum_{n=0}^{l-p} c_n z^{-n}$. Our integration will now be carried out in the complex z-plane rather than the ρ-plane, although the strategy is essentially the same. We define z_∞ to be a large real number $\texttt{scale}*|\sigma\rho_B|$, and obtain initial data approximate to $\{W_l(z_\infty), W_l'(z_\infty)\}$ via evaluation of the truncated series and its z derivative at z_∞. Even for large l we have typically chosen $l-p=5$ terms to define the truncated series. Then to compute $W_l(\sigma\rho_B)$, we must numerically integrate the ODE (34) from z_∞ to $z_B=\sigma\rho_B$ along some path in the complex z-plane. A possible two-component path is shown in Fig. 4. It is composed of a straight ray followed by a circular arc, with the terminal point of the ray being the real z-point $|\sigma\rho_B|$. The arc subtends an angle equal to the argument of σ. If σ happens to lie in the third quadrant, then the relevant two-component path looks like the one in Fig. 4 except reflected across the $\mathrm{Re}\,z$ axis.

Evaluation of the Heun function $W_l(\sigma\rho_B;\sigma)$ features numerical integration of the ODE (32) from z_∞ to $z_B=\sigma\rho_B$ along the same two-component path. Although z of course changes along the integration path, the σ in $W_l(z;\sigma)$ remains fixed throughout the integration. We are then integrating a *different* ODE for each value of σ. Since these Heun functions are not bispectral (see the discussion in Section 2.2.3), there would seem no way around such a cumbersome approach. Were we only interested in $W_l(\sigma\rho_B)$, and not $W_l(\sigma\rho_B;\sigma)$ as well, such an approach would be unnecessary (for then we could integrate with respect to frequency σ). In essence our two-component path method for evaluation of either $W_l(\sigma\rho_B)$ or $W_l(\sigma\rho_B;\sigma)$ is an integration with respect to radius rather than frequency. Indeed, even for the Bessel case, we connect each z_B to the point z_∞ by its own integration path, and during the integration do not record values for $W_l(z)$ along the

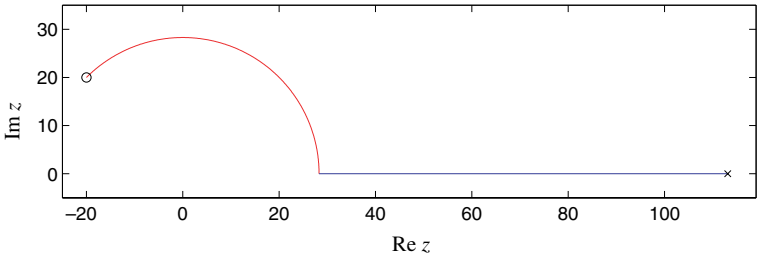

Fig. 4. Two-component path in z-plane. The figure depicts the ray-and-arc path described in the text. Here we have $\rho_B=20$, $\sigma=-1+\mathrm{i}$, and $\texttt{scale}=4$, so that $z_B=-20+\mathrm{i}20$ (marked by an ○) and $z_\infty=4*20*\sqrt{2}\simeq 113$ (marked by an ×). Typically $\texttt{scale}$ will be much larger, but the value here makes for a good figure.

path. Recording such values throughout the integration would be a more efficient way of mapping out the σ dependence of $W_l(\sigma\rho_B)$.

Let us note two key features of two-component paths. First, for any choice of $z_B \neq 0$ the associated path avoids the origin where the function $W_l(z)$ is singular. Second, considering two terminal points, one z_B^a just above and the other z_B^b just below the negative real axis, we note that the respective two-component paths connecting them to z_∞ are mirror images, as depicted in Fig. 5. Therefore, the path leading from z_∞ to z_B^a is globally different than the path leading from z_∞ to z_B^b, this being true despite the fact that z_B^a and z_B^b may lie arbitrarily close to each other in the z-plane. For $l \in \mathbb{Z}_{\geqslant 0}$ the functions $W_l(z)$ are clearly analytic on the punctured z-plane, so that $W_l(z_B^a) = W_l(z_B^b)$ in the limit that these points meet on the negative $\mathrm{Re}\, z$ axis. However, for Heun functions we shall find $W_l(z_B^a;\sigma^a) \neq W_l(z_B^b;\sigma^b)$, and in turn $W_l(\sigma^a\rho_B;\sigma^a) \neq W_l(\sigma^b\rho_B;\sigma^b)$, for corresponding $\sigma^a = z_B^a/\rho_B$ and $\sigma^b = z_B^b/\rho_B$. Therefore, the negative $\mathrm{Re}\,\sigma$ axis is a branch cut for $W_l(\sigma\rho_B;\sigma)$ as a function of σ. Our path choices for connecting points in the second and third quadrants to z_∞ put this branch cut on the negative $\mathrm{Re}\,\sigma$ axis.

As we demonstrate below, the described two-component path method is quite accurate for low l. However, for large l and some values of σ there is a considerable loss of precision associated with evaluating $W_l(\sigma\rho_B)$ by this method (this is true no matter what integration scheme is used along the path components). Therefore, we shortly introduce a more accurate method based on one-component paths. Before turning to the improved method, let us first heuristically describe the trouble the two-component method can run into for large l. In Fig. 6 we graphically demonstrate the breakdown in the method which occurs (for the specified parameter values) when l gets beyond 70. The relevant task under consideration is to obtain $W_l(\sigma\rho_B)$ in a region around those zeros of $W_l(\sigma\rho_B)$ which have large negative real parts. On the LHS we plot $\log|W_{70}(15\sigma)|$, using the logarithm to distribute contour lines more evenly. For the portion of the σ-plane shown only two of seventy zero locations are evident. Note the onset of degradation in the numerical solution. On the RHS we plot $\log|W_{74}(15\sigma)|$, and in the plot two of 74 zero locations are somewhat evident, despite significant degradation. This degradation stems from the following phenomena. Although they do avoid the origin, two-component integration paths, especially those which terminate near a zero with large negative real part, tend to pass through a region near the origin where the solution is quite large. The phenomena become more pronounced as l grows. Two-component paths connect z_∞ (where the solution is of order unity) to z_B (which might be at or near a zero of the solution in question), and at each of these points the solution is in some sense small. Therefore, loss of accuracy is an issue if the connecting path indeed passes through a large-solution region. We document an instance of this situation in Fig. 7.

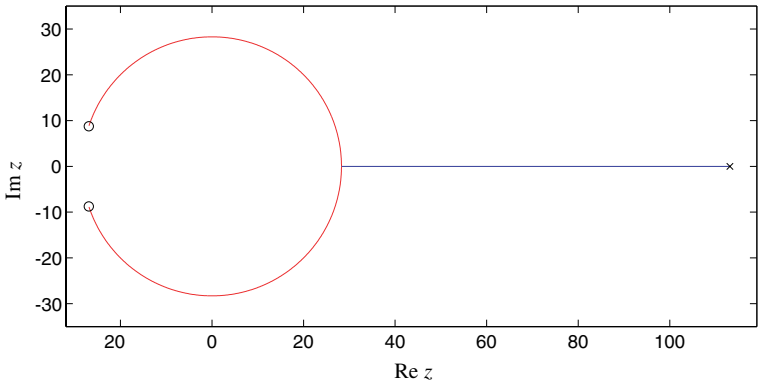

Fig. 5. Mirror image paths. The figure depicts the two globally different paths connecting z_∞ to z-points above and below the negative $\mathrm{Re}\, z$ axis. Use of such different paths puts a branch cut on the negative $\mathrm{Re}\, z$ axis for Heun functions and for Bessel functions not of half-integer order.

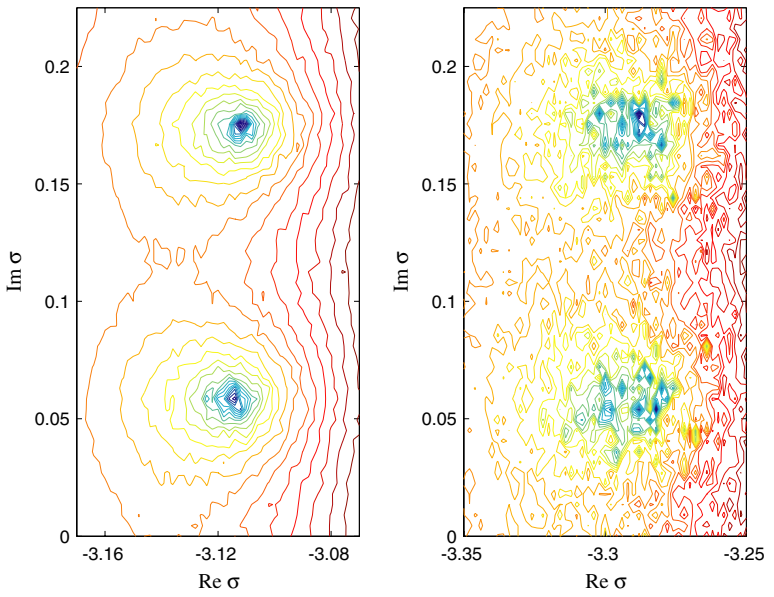

Fig. 6. Contour lines of $\log|W_l(15\sigma)|$ on σ-plane for $l = 70$ and 74. On the LHS we plot $\log|W_{70}(15\sigma)|$. The method used to generate this plot is the one based on two-component paths, and the integration scheme along each path component is fifth-order Runga–Kutta–Fehlberg [58]. Relevant parameters here are $I = 50$, $J = 50$, $N = 49152$, $M = 49152$, $l = 70$, $\rho_B = 15$, $\texttt{scale} = 500$, $p = 65$, and $\kappa = 1$. I and J respectively specify the vertical and horizontal discretization of the σ-plane. N and M are respectively the number of integration steps along the ray and arc. Other parameters are described in the text. On the RHS $l = 74$ rather than 70 and $p = 69$ rather than 65 (the initial condition is still determined by $5 = l - p$ terms). All other parameters are the same as for the LHS plot.

3.1.3. One-component path integration

We now describe an alternative class of integration paths tailored to mitigate the problem of passing through regions where the solution is large. Members of this alternative class are one-component paths, and this new class yields an improved version of the integration method based the two-component paths. As the new method will be more accurate, we will use it to quantify the accuracy of the two-component method.

The one-component paths of interest are essentially dilations of a certain curve $\mathscr{C}$ depicted in Fig. 8. A parametric description of $\mathscr{C}$ in terms of transcendental functions is given in the figure caption. The curve $\mathscr{C}$ is intimately related to the zeros of $W_l(z)$, also the zeros of the MacDonald function $K_{l+1/2}(z)$. As a degree-l polynomial in inverse z, the function $W_l(z)$ has l zeros. Let $n \in \mathbb{Z}_{\geqslant 0}$ run from 1 to l (with $n = 0$ if $l = 0$) and $k_{l,n}$ denote the zeros of $W_l(z)$. It is known that the scaled zeros $(l + 1/2)^{-1}k_{l,n}$ lie arbitrarily close to $\mathscr{C}$ as l becomes large (see results listed or summarized in [19,22,54,55]). Therefore, for a given l, dilation of $\mathscr{C}$ by $l + 1/2$ yields a curve on which the solution $W_l(z)$ tends to remain small. Our one-component integration paths are quartic approximations to (dilations of) $\mathscr{C}$, and an example is depicted in Fig. 9. The approximation is given parametrically by $R(g(\eta), \eta)$, where R is fixed and $g(\eta) = a\eta^4 + b\eta^2 + c$ is a quartic polynomial such that upon multiplication by R the $\mathscr{C}$ points $(0, \pm 1)$, $(x_1, \pm y_1)$, and $(x_0, 0)$ all lie on the parametric approximation. We have $x_1 = -\sqrt{2/(e^2+1)}$, $y_1 = \sqrt{2/(e^2-1)}$, and $x_0 = -\sqrt{\lambda_0^2 - 1}$ with $\lambda_0 \simeq 1.1997$ obeying $\tanh(\lambda_0) = 1/\lambda_0$. From the parametric description of $\mathscr{C}$ given in the caption of Fig. 8, one may verify that each of these points indeed lies on $\mathscr{C}$. Numerically then $a \simeq 0.1534$, $b \simeq 0.5093$, and $c \simeq -0.6627$.

We repeat the graphical investigation described and carried out at the end of Section 3.1.2, but now with the one-component method. The relevant contour plots of $\log|W_{70}(15\sigma)|$ and $\log|W_{74}(15\sigma)|$ are shown in Fig. 10. Comparing this set of plots with the corresponding set in Fig. 6, we see significantly less degradation

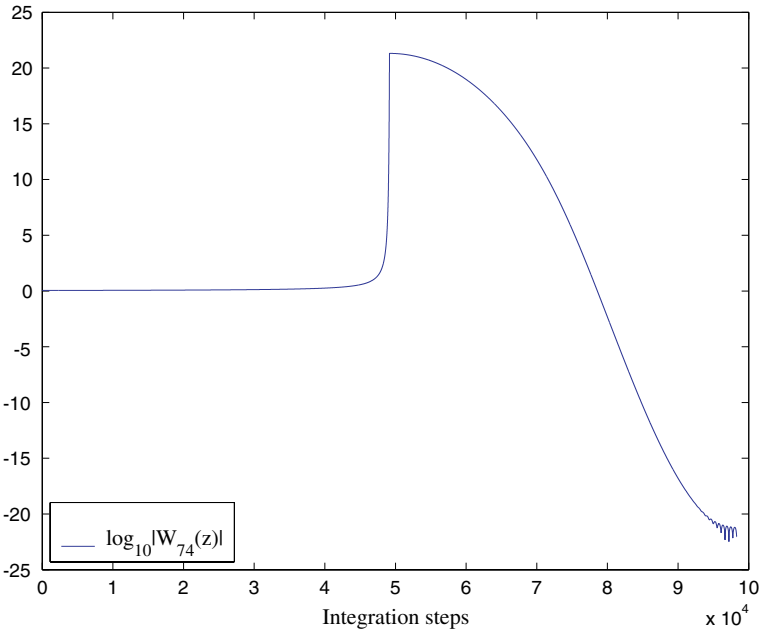

Fig. 7. Value of $\log_{10}|W_{74}(z)|$ along two-component path from z_∞ to $z_B = 15\sigma$ for $\sigma = -3.29128 + i0.05785$. The point $-3.29128 + i0.05785$ is close to a zero of $W_{74}(15\sigma)$ and lies in the region of the σ-plane shown in Fig. 6. The parameters here are the same as those listed in the caption of Fig. 6. Along the horizontal axis we have the $N + M = 98304$ integration steps. The function is of order unity at z_∞ and close to zero at the terminal point z_B. However, note that the modulus of $W_{74}(z)$ gets larger than 10^{20} during the integration.

in former set. Moreover, we again investigate the size of the solution along an integration path in Fig. 11. These figures and their captions argue that the method based on one-component paths is more accurate than the one based on two-component paths, at least insofar as zero-finding is concerned.

3.1.4. Accuracy of the numerical evaluation

To check the accuracy of our methods for evaluating either $W_l(\sigma\rho_B;\sigma)$ or $W_l(\sigma\rho_B)$ we may compare values obtained independently from one-component path and two-component path integration. For the evaluation of $W_l(\sigma\rho_B)$ there are other checks. First, numerical values for $W_l(\sigma\rho_B)$ can be checked against direct evaluations of $\sum_{n=0}^{l} c_n(\sigma\rho_B)^{-n}$. However, as we have seen in (42), for large l the final coefficient c_l and the ones just before it quickly become too large to faithfully evaluate this exact expression. One can use extended precision (say in MATHEMATICA) to get around this problem. Another check, useful for large l even without extended precision, involves the known continued fraction expansion

$$z\frac{W_l'(z)}{W_l(z)} = -\frac{l(l+1)}{2(z+1)+}\,\frac{(l-1)(l+2)}{2(z+2)+}\cdots\frac{2(2l-1)}{2(z+l-1)+}\,\frac{2l}{2(z+l)}. \tag{62}$$

This formula follows from recurrence relations obeyed by MacDonald functions [22]. It remains valid for non-integer l; however, in this case the RHS of the equation is an infinite continued fraction. Lenz's method may be used to evaluate this continued fraction for any l (see the appendix of [53]). Now, both of our integration methods also return the derivative $W_l'(z_B)$ in addition to $W_l(z_B)$. To see why, let $W = U + iV$ (suppressing the argument and l). In order to integrate the second-order ODE (34) for the complex variable W, we switch to a first-order system of ODE for the real vector $(U^\star, U, V, V^\star)$. The $\star$

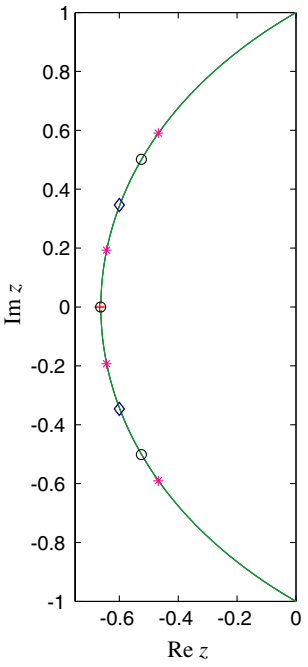

Fig. 8. Asymptotic curve $\mathscr{C}$. The curve is the one described in the text and has parametric form $z(\lambda) = -\sqrt{\lambda^2 - \lambda\tanh\lambda} \pm \mathrm{i}\sqrt{\lambda\coth\lambda - \lambda^2}$ for λ in the domain $[0, \lambda_0]$ with $\lambda_0 \simeq 1.1997$ such that $\tanh\lambda_0 = 1/\lambda_0$. We also plot scaled zeros $(l+1/2)^{-1}k_{l,n}$ for $l = 1, 2, 3, 4$. The cross is the scaled zero of $K_{1/2}(z)$, the diamonds are the scaled zeros of $K_{3/2}(z)$, the circles are the scaled zeros of $K_{5/2}(z)$, and the stars are the scaled zeros of $K_{7/2}(z)$. To the eye these zeros, corresponding as they do to small l values, already lie close to the curve $\mathscr{C}$.

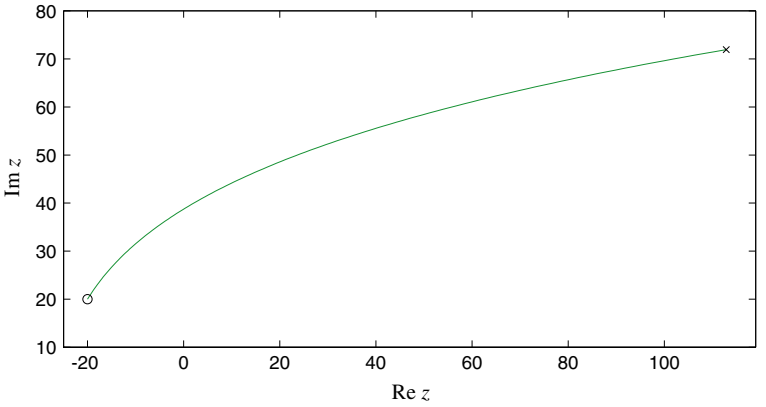

Fig. 9. One-component path. To generate the depicted curve we have set $R \simeq 38.7479$ and chosen η from the range $0.5162 \lesssim \eta \lesssim 1.8650$, ensuring that the terminal point $z_{\mathrm{B}} = 20 + \mathrm{i}20$ and the initial point $z_\infty \simeq 113 + \mathrm{i}72$ (comparable with the analogous point in Fig. 4). For one-component paths the meaning of the `scale` variable is a little different. For such paths the real component of z_∞ is set by $R * \mathtt{scale}$.

denotes differentiation with respect to any relevant path parameter. With knowledge of $U^\star$ and $V^\star$ and the Cauchy–Riemann equations, one can recover W'. Therefore, both the one-component and two-component path methods may also be used to evaluate $z_{\mathrm{B}}W_l'(z_{\mathrm{B}})/W_l(z_{\mathrm{B}})$, and this value can then be

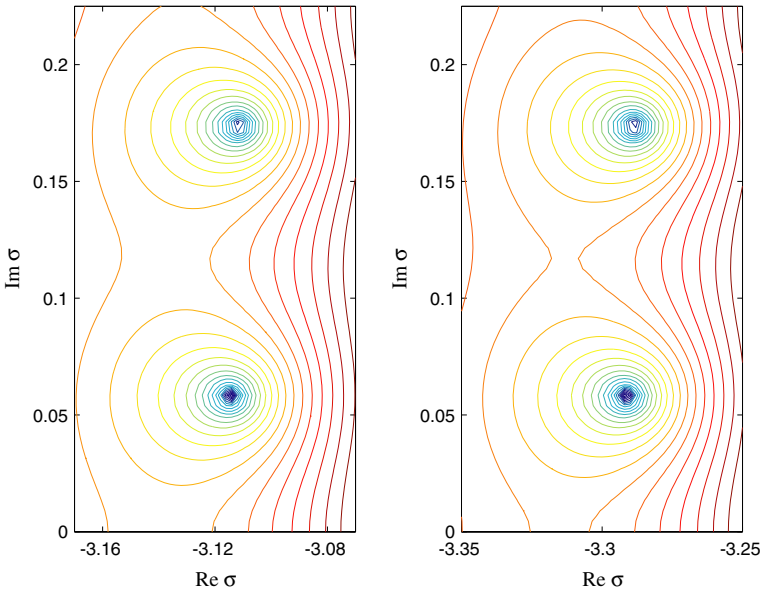

Fig. 10. Contour lines of $\log|W_l(15\sigma)|$ on σ-plane for $l = 70$ and 74. On the LHS we have plotted $\log|W_{70}(15\sigma)|$. The method used to generate the plot is the one based on the one-component paths, again with Runga–Kutta–Fehlberg integration. Relevant parameters here are $I = 50$, $J = 50$, $P = 98{,}304$, $l = 70$, $\rho_B = 15$, `scale` $= 500$, $p = 65$, and $\kappa = 1$. P is the number of subintervals for the numerical integration. Other parameters are described in the text or the caption for Fig. 6. The plot on the RHS is nearly the same, except that now $l = 74$ and $p = 69$ (i.e. the initial condition still determined by $5 = l - p$ terms). All other parameters are the same as for the LHS plot.

checked against the continued fraction (62) evaluated at z_B. In this context, notice that the zeros in σ of the reciprocal $W_l(\sigma\rho_B)/(\sigma\rho_B W_l'(\sigma\rho_B))$ are also the zeros of $W_l(\sigma\rho_B)$, owing to the fact that the zeros of the MacDonald function are simple [22]. Appealing to the above checks, we find that even the inferior numerical method based on two-component paths is quite accurate for $l \leqslant 10$; and we offer the following concrete investigations to sharpen this statement. [11]

Accuracy in zero-finding. The function $W_{10}(15\sigma)$ has 10 zeros, which come in five complex-conjugate pairs. Using the secant algorithm, we compute the five zeros with positive imaginary parts via our two independent methods. Note that whether the one-component or two-component path method is used, each function call in the secant algorithm involves a numerical integration. The results, listed in Table 2, indicate that for low l the two-component path method is associated with absolute errors equal to or better than 10^{-12}, at least insofar as zero-finding is concerned. [12] We reach the same conclusion upon computing the zeros of the Heun function $W_{10}(15\sigma;\sigma)$ via the two methods. This is remarkable in that there is no *a priori* relationship between the asymptotic curve $\mathscr{C}$ and the zeros in σ of the Heun function $W_l(\sigma\rho_B;\sigma)$. However, carrying out the same graphical experiments for Heun functions that we carried out for Bessel functions and documented in Figs. 7 and 11, we again find that the one-component path method is better than the two-component path method at keeping the solution small during the integration. Numerical experiments described in Section 4.1.1 further clarify this issue.

[11] We remark that these accuracy checks test our methods where we need them most, that is on those tasks necessary for a numerical construction the kernel via the representation (55).

[12] Computing the same zeros in extended precision with MATHEMATICA, we have checked that the one-component path method yields the zeros with absolute errors near 10^{-15}.

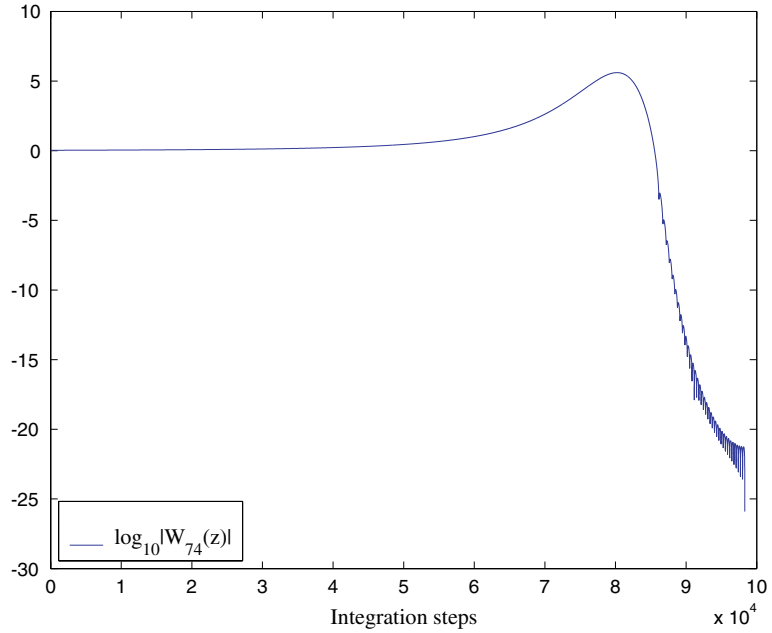

Fig. 11. Value of $\log_{10}|W_{74}(z)|$ along one-component path from z_∞ to $z_B = 15\sigma$ for $\sigma = -3.29128 + \mathrm{i}0.05785$. The point $-3.29128 + \mathrm{i}0.05785$ is close to a zero of $W_{74}(15\sigma)$ and lies in the region of the σ-plane shown in Fig. 10. Along the horizontal axis we have the $P = 98{,}304$ integration steps. Note that the modulus of $W_{74}(z)$ never gets so large as it does in Fig. 7.

Table 2
Zeros of $W_{10}(15\sigma)$ computed via two different methods

$-0.461469660361894 + \mathrm{i}0.057844346363414$
$-0.441019397698505 + \mathrm{i}0.174104528053357$
$-0.397835221905874 + \mathrm{i}0.292329812596140$
$-0.325747971123938 + \mathrm{i}0.414999032164771$
$-0.207261082243274 + \mathrm{i}0.548846630604906$
$-0.461469660361817 + \mathrm{i}0.057844346363415$
$-0.441019397698458 + \mathrm{i}0.174104528053339$
$-0.397835221905853 + \mathrm{i}0.292329812596129$
$-0.325747971123933 + \mathrm{i}0.414999032164771$
$-0.207261082243273 + \mathrm{i}0.548846630604906$

In the top table we list five of the 10 zeros (the other five are complex conjugates). These have been found using the two-component path method in tandem with the secant algorithm. In the second table we list the same zeros, now found using the one-component path method with the secant algorithm.

Accuracy in the cut profile. As applied to the Heun case, both the two-component and one-component path methods also return $W_l'(\sigma\rho_B;\sigma)$. This can be seen via argumentation similar to that given above in the context of the real vector $(U^\star, U, V, V^\star)$. Therefore, we have two independent methods for calculating $\sigma\rho_B W_l'(\sigma\rho_B;\sigma)/W_l(\sigma\rho_B;\sigma)$, where σ may be chosen pure real and negative (say with the convention that all paths approach the negative $\mathrm{Re}\,\sigma$ axis running through the second quadrant). That is to say, each of our methods may be used to evaluate the cut profile

$$f_l(\chi;\rho_B) = \mathrm{Im}\left[\mathrm{e}^{\mathrm{i}\pi}\chi\rho_B W_l'(\mathrm{e}^{\mathrm{i}\pi}\chi\rho_B;\mathrm{e}^{\mathrm{i}\pi}\chi)/W_l(\mathrm{e}^{\mathrm{i}\pi}\chi\rho_B;\mathrm{e}^{\mathrm{i}\pi}\chi)\right]. \tag{63}$$

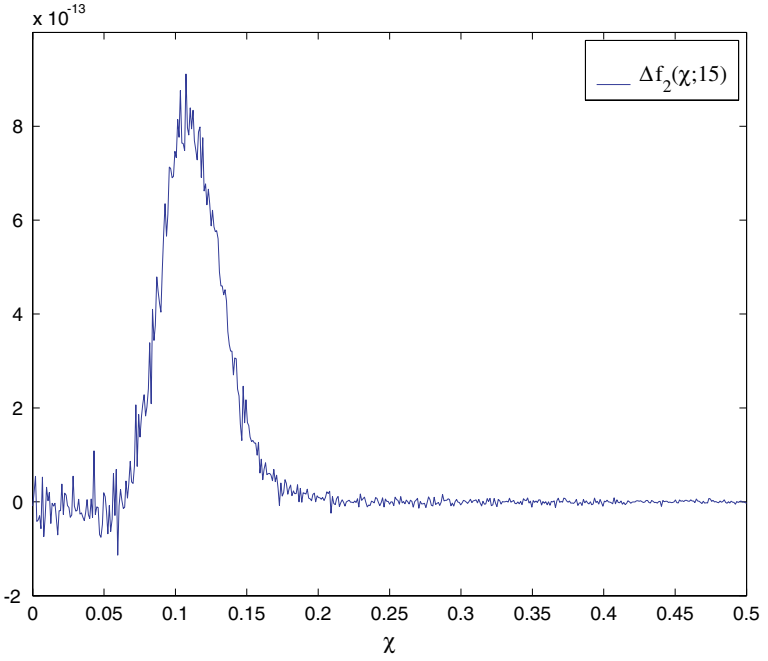

Fig. 12. Absolute error in the cut profile $f_2(\chi;15)$. Here we plot the difference $\Delta f_2(\chi;15)$ of two numerical computations of $f_2(\chi;15)$, one based on the two-component path method and the other on the one-component path method. For the two-component method we have $N = 131{,}072 = M$, while for the one-component method $P = 262{,}144$. Parameters common to both computations are $\kappa = 1$, $\texttt{scale} = 1000$ and $p = -3$ so $l - p = 5$. There are 512 χ-subintervals in the plot.

Using each method to obtain its own numerical graph for the profile $f_2(\chi;15)$ shown in Fig. 3 of Section 2.4.2, we then plot the difference of these graphs in Fig. 12. Similar graphs for other values of $l \leqslant 10$ indicate that the two-component path method evaluates the maximum value of $|f_l(\chi;15)|$ with an absolute error better than 10^{-10}. For the following reasons we believe that the one-component path method computes this maximum with an even smaller absolute error. The essential support of $|f_l(\chi;15)|$ corresponds to a region of the σ plane near those zeros of $W_l(\sigma\rho_B;\sigma)$ with largest negative real part. Therefore, in connecting z_∞ to a purely real $z_B = \exp(i\pi)\chi\rho_B$ on the cut, a one-component path runs all the way near (a dilation of) $\mathscr{C}$, indicating that the numerical solution along such a one-component path again tends to remain small. Experiments like those documented in Figs. 7 and 11 confirm this expectation.

We will mainly use the described integration methods for small $l \leqslant 10$. However, we note that via comparison with both the continued fraction expression and extended precision calculations in MATHEMATICA, we believe that our one-component path method maintains single precision accuracy up to about $l = 50$, at least insofar as zero-finding is concerned. Finally, we mention that we have carried out all integration using the Runga–Kutta–Fehlburg scheme with fixed step-size along individual path components. In light of the sufficient accuracy noted here and the next subsection, we have not found it necessary to introduce any sort of adaptive integration. Furthermore, we have not found the local truncation error estimate (stemming from comparison between the fourth- and fifth-order integration schemes) provided by Runga–Kutta–Fehlburg to be a useful diagnostic for our purposes. Relying on our own accuracy checks, we have simply used the straight explicit fifth-order scheme.

3.2. Numerical evaluation of the radiation kernel

The numerical methods discussed in the last subsection work well for values of $l \leqslant 10$, and via (55) will allow us to directly construct sufficiently accurate sum-of-poles representations of the FDRK. Moreover, even for moderately large l these methods prove useful in qualitative investigations of the outgoing solution's analytic structure. However, when it comes to building an accurate sum-of-pole representation of the FDRK for high l, the described methods lack the necessary accuracy.

In this subsection we describe different methods for direct evaluation of the radiation kernel itself along the $\mathrm{Im}\,\sigma$ axis, ones sufficiently accurate even for high l. Given accurate profiles for the real and imaginary parts of the radiation kernel along this axis, we may then extract an accurate sum-of-poles representation via a method described in detail in Section 1.2 of [2] and due to [19]. Here we described two methods for evaluating $\hat{\omega}_l(\sigma;\rho_{\mathrm{B}})$ when σ is pure imaginary, one accurate so long as $|\sigma| \gg 0$ and the other so long as $0 \neq |\sigma| \lesssim 1$. There is some interval of overlap on the $\mathrm{Im}\,\sigma$ axis on which both methods are accurate and may be compared. We warn the reader that we also use the notation $\hat{\omega}_l(\sigma;\rho_{\mathrm{B}})$ for the Bessel FDRK $\sigma\rho_{\mathrm{B}}W_l'(\sigma\rho_{\mathrm{B}})/W_l(\sigma\rho_{\mathrm{B}})$. In order to avoid the confusion which might arise from this dual meaning of the symbol $\hat{\omega}_l(\sigma;\rho_{\mathrm{B}})$, in this subsection we sometimes adopt the following notation. For the product of z with the Heun logarithmic derivative we may use

$$w_l(z;\sigma) = zW_l'(z;\sigma)/W_l(z;\sigma), \tag{64}$$

while for the corresponding Bessel object we may use

$$w_l(z) = zW_l'(z)/W_l(z). \tag{65}$$

Formally $w_l(z) = w_l(z;0)$, in parallel with conventions in Section 2.3.2. For the Heun case $\hat{\omega}_l(\sigma;\rho_{\mathrm{B}}) = w_l(\sigma\rho_{\mathrm{B}};\sigma)$, while for the Bessel case $\hat{\omega}_l(\sigma;\rho_{\mathrm{B}}) = w_l(\sigma\rho_{\mathrm{B}})$.

3.2.1. Evaluation of the kernel for large imaginary frequencies

We turn first to the evaluation of $\hat{\omega}_l(\sigma;\rho_{\mathrm{B}})$ for $\sigma \in \mathrm{i}\mathbb{R}$ and $|\sigma| \gg 0$. For the remainder of this subsection $\sigma = \mathrm{i}y$ for real y. In this scenario we find it useful to again work with the complex variable $z = \sigma\rho$. As before, for a given σ the terminal evaluation point will be denoted by $z_{\mathrm{B}} = \sigma\rho_{\mathrm{B}}$, and it lies on the $\mathrm{Im}\,z$ axis. Consider two positive real numbers $\mathtt{scale}_1 > \mathtt{scale}_2$ and associated z-points $z_1 = \mathtt{scale}_1 + z_{\mathrm{B}}$ and $z_2 = \mathtt{scale}_2 + z_{\mathrm{B}}$. The point z_1 is analogous to the point z_∞ introduced before. Further consider a straight path like the one shown in Fig. 13 running through all of these points. Let us now outline the method for obtaining the value $\hat{\omega}_l(z_{\mathrm{B}}/\rho_{\mathrm{B}};\rho_{\mathrm{B}})$, mostly considering only the model Bessel case to streamline the presentation. First, using the truncated series $\sum_{n=0}^{l-p} c_n z_1^{-n}$, we compute initial values for the ODE (34). Next, we integrate the ODE along the straight path from z_1 to z_2 (the first portion of the path in Fig. 13). As $\mathrm{Re}\,z > 0$ along this path, we again have exponential suppression of errors both in the initial conditions and due to roundoff. The result of this integration is accurate numerical values for $W_l(z_2)$ and $W_l'(z_2)$, from which we can directly build a numerical value for the kernel $z_2W_l'(z_2)/W_l(z_2)$ at this intermediary point. The assumption here is that z_2 is still large enough in modulus to ensure that the solution $W_l(z_2)$ is not too large. Finally, we integrate the radiation kernel itself along the straight path from z_2 to z_{B}, carrying this out as follows.

Whether we are working with (32) or (34), we have an ODE of the form

$$\frac{\mathrm{d}^2\hat{\Phi}_l}{\mathrm{d}z^2} + R(z;\sigma)\frac{\mathrm{d}\hat{\Phi}_l}{\mathrm{d}z} + S(z;\sigma)\hat{\Phi}_l = 0, \tag{66}$$

so that both $w_l(z)$ and $w_l(z;\sigma)$ obey a first-order nonlinear ODE of the form

$$\frac{\mathrm{d}w_l}{\mathrm{d}z} - \frac{w_l}{z} + \frac{w_l^2}{z} + R(z;\sigma)w_l + zS(z;\sigma) = 0. \tag{67}$$

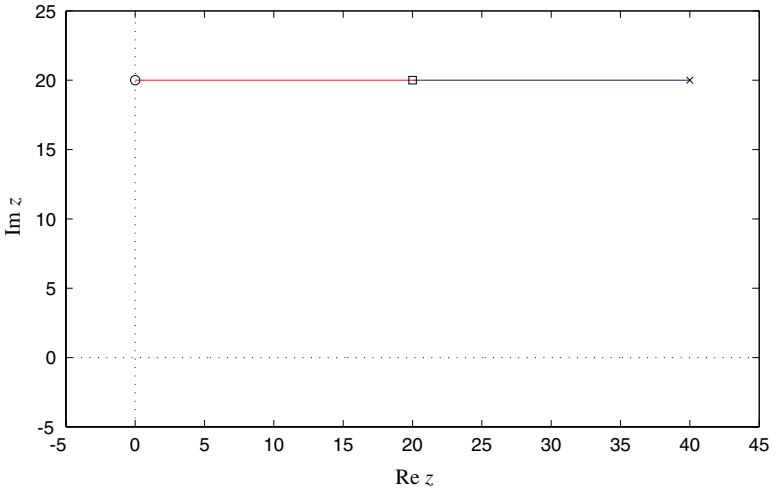

Fig. 13. Two-component path in z-plane. The figure depicts a straight path of the type described in the text. Here we have $\rho_B = 20$, $\sigma = \mathrm{i}$, $\mathtt{scale}_1 = 20$, and $\mathtt{scale}_2 = 40$, so that the points z_1, z_2 and z_B respectively correspond to the marked cross, square, and circle. Typically $\mathtt{scale}_1$ and $\mathtt{scale}_2$ will be much larger, but the values here make for a good figure.

We use the same symbol w_l as the dependent variable here, since as a first-order ODE there is only one linearly independent solution. With the accurate value for $w_l(z_2)$ at our disposal at the end of the first integration leg, we integrate this last ODE from z_2 to the terminal value z_B (the second portion of the path in Fig. 13) in order to obtain the desired complex value $w_l(z_B) = z_B W_l'(z_B)/W_l(z_B)$. For the Heun case Eq. (67) is an ODE for $w_l(z;\sigma) = zW_l'(z;\sigma)/W_l(z;\sigma)$, and it is again integrated from z_2 to z_B, given an accurate value for $w_l(z_2;\sigma)$.

The method just described is unstable if the terminal point z_B lies too close to the origin. Indeed, notice that some of the terms in the ODE (67) are singular at the origin, showing that finiteness of the kernel derivative at the origin depends on exact cancellation of singular terms. Round off error will spoil any such exact cancellation in an integration towards a terminal z_B equal to or near zero. Later we demonstrate that the value $\hat{\omega}_l(0;\rho_B)$ of the kernel at the origin can be computed in closed form for both Bessel and Heun cases. This raises the possibility that the value $w_l(z_B)$ – or in the Heun case the value $w_l(z_B;\sigma)$ – corresponding to a non-zero $|z_B| \ll 1$ might be numerically computed via integration of (67) out from the origin. However, as discussed in [1] this seems not a viable approach.

3.2.2. Evaluation of the kernel for small imaginary frequencies

For the reasons just laid down, we use a different method for small *non-zero* imaginary σ. The new method employs integration in the complex ρ-plane rather than the z-plane. We introduce new positive real numbers $\mathtt{scale}_1 > \mathtt{scale}_2 > \rho_B$, a phase factor $\exp(\mathrm{i}\theta)$, and the following associated ρ-points (all in polar form): $\rho_1 = \mathtt{scale}_1 * \exp(\mathrm{i}\theta)$, $\rho_2 = \mathtt{scale}_2 * \exp(\mathrm{i}\theta)$, $\rho_3 = \rho_B \exp(\mathrm{i}\theta)$, and ρ_B. These points define a three-component path in the ρ-plane such as the one shown in Fig. 14. Let us now outline the new method for computing the value $\hat{\omega}_l(\sigma;\rho_B)$, again mostly considering only the model Bessel case to streamline the presentation. First, using the asymptotic expansion (61), we compute initial values for the ODE (60). Next, we integrate (60) along the straight ray from ρ_1 to ρ_2 (the first portion of the path in Fig. 14). We choose the angle θ such that $\mathrm{Re}\,(\sigma\rho) > 0$ along this path, ensuring exponential suppression of errors both in the initial conditions and due to roundoff. The result of this integration is accurate numerical values for $W_l(\sigma\rho_2)$ and $W_l^{\rho}(\sigma\rho_2)$, from which we can directly build a numerical value for $w_l(\sigma\rho_2)$ at the intermediary point ρ_2. Similar to before, the assumption here is that ρ_2 is large enough in modulus to ensure that the solution $W_l(\sigma\rho_2)$ is not too large. Finally, we integrate $w_l(\sigma\rho)$ itself along a two-component ray-and-arc path from ρ_2

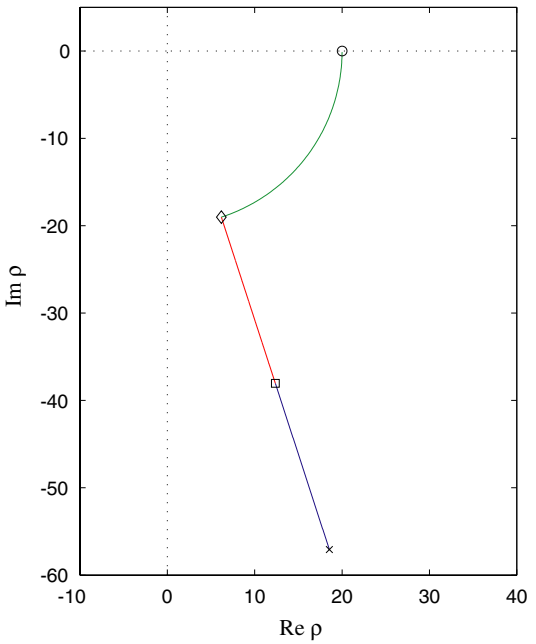

Fig. 14. Three-component path in ρ-plane. The figure depicts an example three-component path of the type described in the text. Here we have $\rho_B = 20$, $\texttt{scale}_1 = 60$, $\texttt{scale}_2 = 40$, and $\theta = -2\pi/5$ so that the points ρ_1, ρ_2, ρ_3 and ρ_B respectively correspond to $60\exp(-i2\pi/5)$ ($\times$), $40\exp(-i2\pi/5)$ ($\Box$), $20\exp(-i2\pi/5)$ ($\Diamond$), and 20 ($\bigcirc$). The depicted path corresponds to a σ value lying on the positive imaginary axis, so that between ρ_1 and ρ_3 we have $\mathrm{Re}\,(\sigma\rho) > 0$. Better suppression of error would be had for $\theta = -\pi/2$, in which case the portion of the path between ρ_1 and ρ_3 would lie on the negative imaginary axis. However, in this case the final integration would be over a longer arc, and on this final arc we do not expect to have error suppression. There seems to be some trade-off here, so we have kept θ as a parameter. In any case, typically $\texttt{scale}_1$ and $\texttt{scale}_2$ will be much larger, but the values here make for a good figure.

to the real point ρ_B, by way of an intermediate point ρ_3. Such a remaining two-component path is depicted in Fig. 14 as the final two portions of the curve connecting ρ_2 to ρ_B. This integration is carried out as follows.

Whether we are working with (31) or (60), we have an ODE of the form

$$\frac{d^2\hat{\Phi}_l}{d\rho^2} + \mathscr{R}(\rho;\sigma)\frac{d\hat{\Phi}_l}{d\rho} + \mathscr{S}(\rho;\sigma)\hat{\Phi}_l = 0, \tag{68}$$

whence both $w_l(\sigma\rho;\sigma)$ and $w_l(\sigma\rho)$ obey a first-order nonlinear ODE of the form

$$\frac{dw_l}{d\rho} - \frac{w_l}{\rho} + \frac{w_l^2}{\rho} + \mathscr{R}(\rho;\sigma)w_l + \rho\mathscr{S}(\rho;\sigma) = 0. \tag{69}$$

To reach this equation, we have used, for example, $w_l(\rho\sigma) = \rho W_l^{\rho}(\rho\sigma)/W_l(\rho\sigma)$. Given the initial value for $w_l(\sigma\rho_2)$ obtained from the first leg of the integration in the last paragraph, we first integrate (69) along the straight ray from ρ_2 to ρ_3 which has the same modulus as the terminal point ρ_B. The final leg, a rotation back to the $\mathrm{Re}\,\rho$ axis, is an integration of (69) along an arc from ρ_3 to ρ_B.

3.2.3. Value of the kernel at the origin

For the Bessel case the origin value $\hat{\omega}_l(0;\rho_B)$ of the radiation kernel is the limit $\lim_{\sigma\to 0} w_l(\sigma\rho_B)$, while for the Heun case the value $\hat{\omega}_l(0;\rho_B)$ is the limit $\lim_{\sigma\to 0} w_l(\sigma\rho_B;\sigma)$. Whether considering the Bessel or Heun case, we may derive an exact expression for the value $\hat{\omega}_l(0;\rho_B)$. Turn first to the Bessel case, where

$W_l(\sigma\rho) = \sum_{n=0}^{l} c_n(\sigma\rho)^{-n}$ is of course singular at $\sigma = 0$. However, with this exact expression it is easy to check that

$$\lim_{\sigma\to 0} w_l(\sigma\rho_{\mathrm{B}}) = -l. \tag{70}$$

We stress that this calculation of $\hat{\omega}_l(0;\rho_{\mathrm{B}})$ makes use of the exact form of the outgoing solution, which is not at our disposal in the Heun case. A separate recipe for getting this value, one without appeal to the exact form of $W_l(\sigma\rho_{\mathrm{B}})$, goes as follows. Set $\sigma = 0$ in (60), thereby reaching an ODE

$$\frac{\mathrm{d}^2\hat{\Phi}_l}{\mathrm{d}\rho^2} - \frac{l(l+1)}{\rho^2}\hat{\Phi}_l = 0 \tag{71}$$

with solutions ρ^{l+1} and ρ^{-l}. We now use $[\rho\partial_\rho \log \rho^{-l}]|_{\rho=\rho_{\mathrm{B}}}$ as the origin value $\hat{\omega}_l(0;\rho_{\mathrm{B}})$, again finding $-l$.

Let us turn to the Heun case and follow this recipe for getting the value $\hat{\omega}_l(0;\rho_{\mathrm{B}})$. We set $\sigma = 0$ in (31), obtaining the following ODE:

$$\frac{\mathrm{d}^2\hat{\Phi}_l}{\mathrm{d}\rho^2} + \left[-\frac{1}{\rho} + \frac{1}{\rho-1}\right]\frac{\mathrm{d}\hat{\Phi}_l}{\mathrm{d}\rho} + \left[\frac{\kappa}{\rho^2} - \frac{\kappa + l(l+1)}{\rho(\rho-1)}\right]\hat{\Phi}_l = 0. \tag{72}$$

Both solutions to this equation may be expressed in terms of infinite series in inverse ρ. The one corresponding to ρ^{-l} above has the form

$$\sum_{n=0}^{\infty} a_n \rho^{-(l+n)}, \tag{73}$$

where $a_0 = 1$ and

$$a_{n+1} = \frac{(l+n)(l+n+2)+\kappa}{(l+n+1)(l+n+2) - l(l+1)}a_n. \tag{74}$$

The series is positive and absolutely convergent for all $\rho > 1$. Elementary calculations then yield

$$\hat{\omega}_l(0;\rho_{\mathrm{B}}) = -\sum_{n=0}^{\infty}(l+n)a_n\rho_{\mathrm{B}}^{-n} \Big/ \sum_{n=0}^{\infty} a_n\rho_{\mathrm{B}}^{-n} \tag{75}$$

as our concrete expression for the value in question. Notice that this value approaches $-l$ in the $\rho_{\mathrm{B}} \to \infty$ limit as expected.

3.2.4. Accuracy of the numerical evaluation

Fig. 15 depicts the real part $u_{64}(15\mathrm{i}y)$ and the imaginary part $v_{64}(15\mathrm{i}y)$ of the Bessel FDRK $\hat{\omega}_{64}(\mathrm{i}y;15) = w_{64}(15\mathrm{i}y)$ along the $\mathrm{Im}\,\sigma$ axis for $l = 64$ and $\rho_{\mathrm{B}} = 15$. We have generated these plots using the methods described in this subsection, and have listed other parameters set while obtaining them in the figure caption. To examine the accuracy of these numerical profiles, we may compare them with corresponding profiles obtained via the continued fraction expansion (62). We consider the profiles stemming from the continued fraction expansion as the "exact" ones. With the two sets of profiles, one may compute corresponding absolute and relative error measures. We plot these errors in Fig. 16. From such plots we conclude that our numerical methods evaluate $w_{64}(15\mathrm{i}y)$ with an absolute supremum error less than 10^{-12} and a relative supremum error less than 10^{-14}, at least for $|y| < 1000$. For the Bessel case at hand we have found comparable error bounds associated with all other values of $l \in \{10, 11, \ldots, 64\}$, although we note that the corresponding y-interval needs to shrink by as much as an order of magnitude to maintain these bounds for $l = 10$.

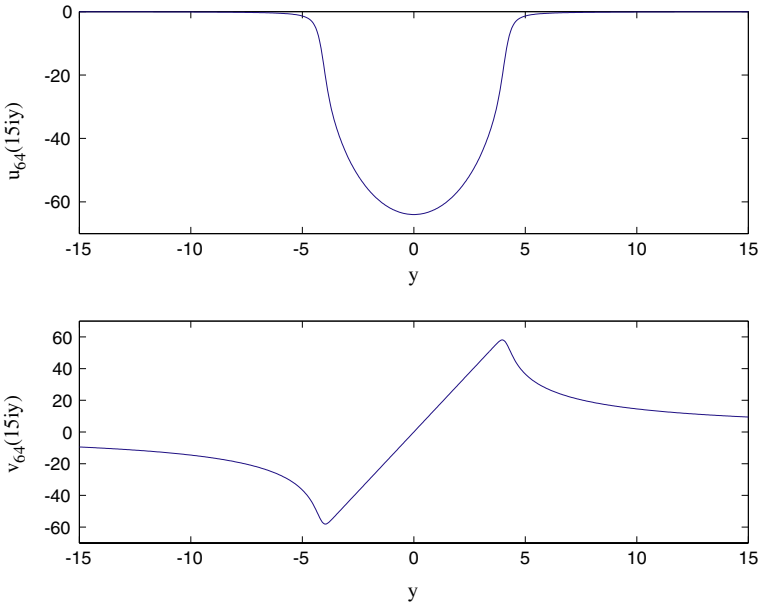

Fig. 15. Bessel FDRK $\hat{\omega}_{64}(\mathrm{i}y;15) = w_{64}(15\mathrm{i}y)$. Here we plot the functions $u_{64}(15\mathrm{i}y) = \mathrm{Re}\ w_{64}(15\mathrm{i}y)$ and $v_{64}(15\mathrm{i}y) = \mathrm{Im}\ w_{64}(15\mathrm{i}y)$, with the y axis split into 512 subintervals. For $|y| > \mathtt{break} = 1$ we have evaluated $\hat{\omega}_{51}(\mathrm{i}y;15)$ using two-component integration with the following parameter values: $N = 131{,}072$, $M = 131{,}072$, $\mathtt{scale}_1 = 1000$, and $\mathtt{scale}_2 = 100$. N and M are respectively the number of integration steps taken along the first and second components of the path. For $|y| \leqslant \mathtt{break}$ we have evaluated $\hat{\omega}_{51}(\mathrm{i}y;15)$ using three-component integration with the parameter values $N = 131{,}072$, $M = 131{,}072$, $P = 2048$, $\theta = \pi/4$, $\mathtt{scale}_1 = 1000$, and $\mathtt{scale}_2 = 100$. N, M, and P are respectively the number of integration steps taken along the first, second, and third components of the path. For both integration methods $\kappa = 1$ and $p = 59$. Typically, we have chosen break smaller, but now have $\mathtt{break} = 1$ to demonstrate the three-component method.

Fig. 17 depicts the real part $u_{64}(15\mathrm{i}y;\mathrm{i}y)$ and the imaginary part $v_{64}(15\mathrm{i}y;\mathrm{i}y)$ of the Heun FDRK $\hat{\omega}_{64}(\mathrm{i}y;15) = w_{64}(15\mathrm{i}y;\mathrm{i}y)$ along the $\mathrm{Im}\,\sigma$ axis. We have again chosen the representative case $l = 64$ and $\rho_{\mathrm{B}} = 15$, setting the rest of the parameters to the same values used to generate the Bessel profiles depicted in Fig. 15. Note that the two sets of profiles are qualitatively very similar. However, they are different. In particular, now the real part has a minimum value of -66.2816976576098 rather than -64. For the Heun case at hand we have no analog of the continued fraction expansion with which to check the accuracy of the profiles. Nevertheless, at least for y values of order unity, we can perform an accuracy check by comparing the two-component and three-component path methods for evaluating the kernel. Such a comparison is shown in Fig. 18. With the two numerically obtained kernels we form an absolute error measure $|\Delta w_{64}(15\mathrm{i}y;\mathrm{i}y)|$ and also a relative error measure $|\Delta w_{64}(15\mathrm{i}y;\mathrm{i}y)|/|w_{64}(15\mathrm{i}y;\mathrm{i}y)|$, over $y \in [0.5, 8]$ for both. In the denominator of the relative error, we happen to have used the kernel stemming from the three-component method. Fig. 18 displays plots of both error measures. Note that poor performance for the three-component method is evident in the right portions of the plots. For the three-component method the length of the third and final integration path grows with y. Therefore, for large y one expects a corresponding loss of precision for the three-component method.

4. Sum-of-poles representation of the radiation kernel

In this section we focus on both exact and approximate representation of the FDRK $\hat{\omega}_l(\sigma;\rho_{\mathrm{B}})$ as a sum of poles. In the first subsection we qualitatively discuss the exact representation (55) of the FDRK as a

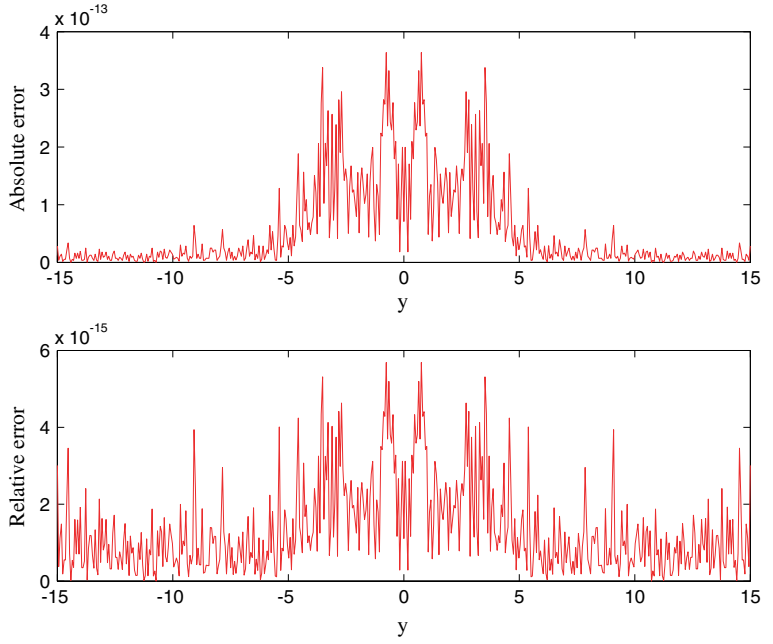

Fig. 16. Error in Bessel FDRK $\hat{\omega}_{64}(\mathrm{i}y;15)$. Here we plot the absolute error $|\Delta w_{64}(15\mathrm{i}y)|$ as well as the relative error $|\Delta w_{64}(15\mathrm{i}y)|/|w_{64}(15\mathrm{i}y)|$. These errors have been computed against the "exact" $w_{64}(15\mathrm{i}y)$ generated with the continued fraction expression (62). Parameters are the same as in Fig. 15.

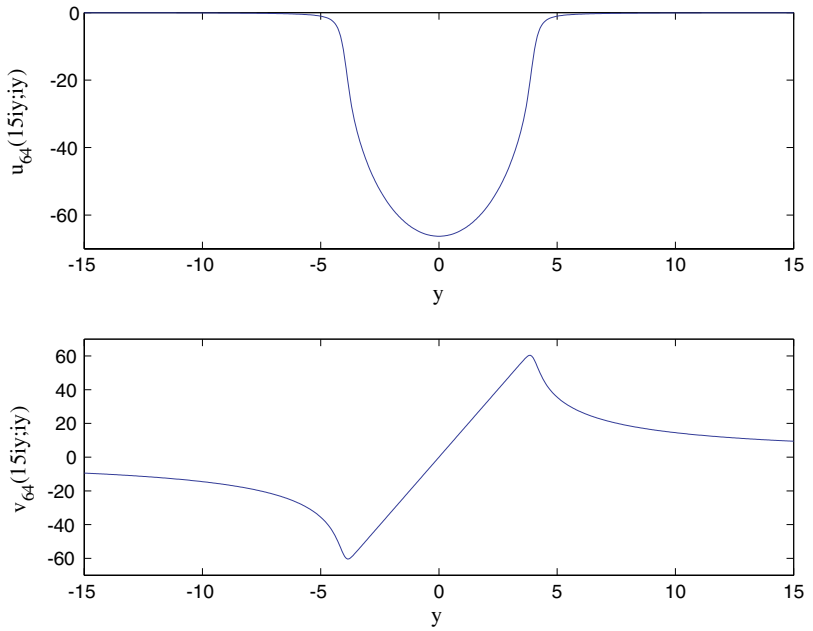

Fig. 17. Heun FDRK $\hat{\omega}_{64}(\mathrm{i}y;15) = w_{64}(15\mathrm{i}y;\mathrm{i}y)$. Here we plot the functions $u_{64}(15\mathrm{i}y;\mathrm{i}y) = \mathrm{Re}\ w_{64}(15\mathrm{i}y;\mathrm{i}y)$ and $v_{64}(15\mathrm{i}y;\mathrm{i}y) = \mathrm{Im}\ w_{64}(15\mathrm{i}y;\mathrm{i}y)$. All parameters in these plots match those listed in Fig. 15 depicting the Bessel FDRK.

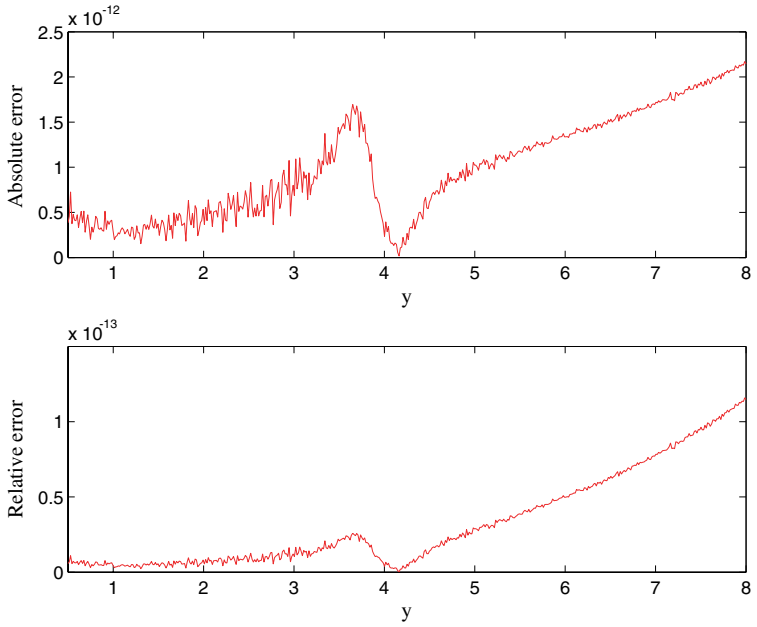

Fig. 18. Error in Heun FDRK $\hat{\omega}_{64}(\mathrm{i}y;15) = w_{64}(15\mathrm{i}y;\mathrm{i}y)$. Here we plot the absolute error measure $|\Delta w_{64}(15\mathrm{i}y;\mathrm{i}y)|$ and the relative error measure $|\Delta w_{64}(15\mathrm{i}y;\mathrm{i}y)|/|w_{64}(15\mathrm{i}y;\mathrm{i}y)|$ described in the text. We have $y \in [0.5, 8]$ for both. All other parameters set in generating these plots are the same as those listed in the caption of Fig. 15.

(continuous and discrete) sum of poles, highlighting what we believe to be its main features. In the second subsection we document our particular numerical construction of the FDRK as a sum of poles, and give an analysis of its numerical error. We stress that from a theoretical standpoint we are *conjecturing* that the Schwarzschild FDRK – built from the Heun function $W_l(z;\sigma)$ – admits the representation (55), although we do provide compelling numerical evidence for a representation of this form. This is in contrast to the case of the flatspace FDRK – built from the Bessel function $W_l(z)$ – which we theoretically know admits such a representation [19]. Since for us the representation (55) of the Schwarzschild FDRK is ultimately conjecture, there is more need to painstakingly justify it numerically, and we do so in the second subsection. This section focuses on the $\jmath = 0$ ($\kappa = 1$) case, but we believe it to be representative.

In this section and in the simulations described in [1,2], we have almost exclusively worked with an outer boundary radius $\rho_{\mathrm{B}} \in [15, 25]$, corresponding to a physical outer boundary radius $r_{\mathrm{B}} \in [30\mathrm{m}, 50\mathrm{m}]$. Therefore, were we considering a more general isolated source of gravitational radiation, one with gravitational radius 2m, then the boundary two-sphere B would be located outside of the *strong-field region* as defined by Thorne [59]. Moreover, for wave simulation on a fixed background as we consider here, the location of B corresponds to a metric coefficient $F(\rho_{\mathrm{B}})$ from (5) in the range $0.9\overline{33} \leqslant F(\rho_{\mathrm{B}}) \leqslant 0.96$. Whence B lies in a region where the Schwarzschild metric is flat up to small correction. Our ROBC described in Section 2.4 are not tied to the weak field region, however, for this region our numerical methods for constructing the FDRK are accurate.

4.1. Qualitative study of pole locations and cut profile

Using the one-component path method described in Section 3.1.3, we first turn to the analytic structure of $W_l(\sigma\rho_{\mathrm{B}};\sigma)$ as a function of frequency σ in the lefthalf plane, assuming that a zero of this function corresponds to a pole location appearing in (55). Using the same method, we then draw some quick

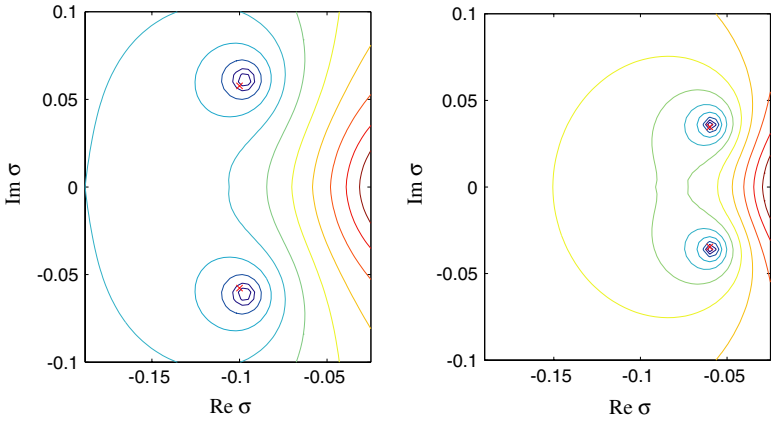

Fig. 19. Zeros of $W_2(15\sigma;\sigma)$ and $W_2(25\sigma;\sigma)$. The left-hand plot shows contour lines of $\log|W_2(15\sigma;\sigma)|$, and the right-hand one shows contour lines of $\log|W_2(25\sigma;\sigma)|$. The logarithm mollifies the singularity at the origin, distributing contour lines more evenly. Notice that the zero locations are closer to the origin in the right-hand plot. In the left-hand plot and the right-hand plot we have also respectively marked as crosses the zeros of the Bessel functions $W_2(15\sigma) = 1 + 3(15\sigma)^{-1} + 3(15\sigma)^{-2}$ and $W_2(25\sigma) = 1 + 3(25\sigma)^{-1} + 3(25\sigma)^{-2}$. Perhaps evident even to the eye, the Bessel and Heun zeros lie closer to each other in the right-hand plot (corresponding to the larger value of ρ_B).

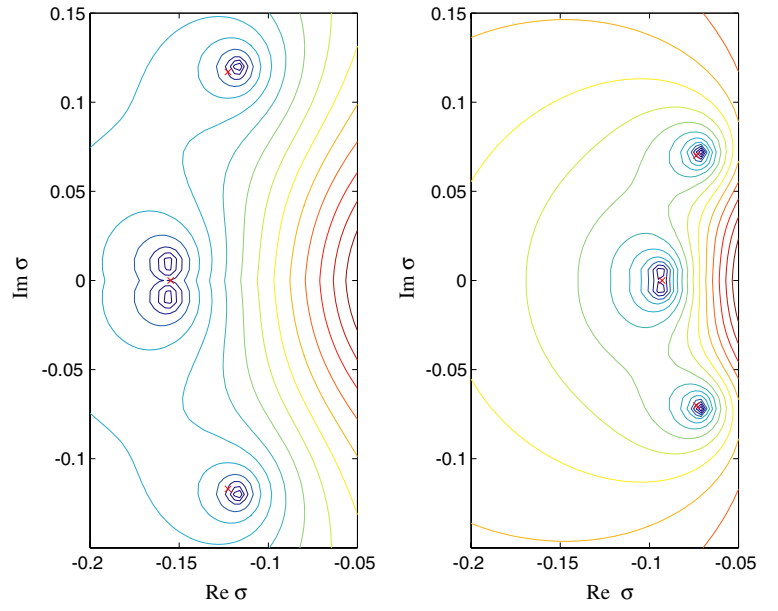

Fig. 20. Zeros of $W_3(15\sigma;\sigma)$ and $W_3(25\sigma;\sigma)$. The left-hand plot shows contour lines of $\log|W_3(15\sigma;\sigma)|$, and the right-hand one shows lines of $\log|W_3(25\sigma;\sigma)|$. Again, crosses mark the corresponding Bessel zeros. Notice in the left-hand plot that the single real Bessel zero corresponds to a pair of zeros in the Heun case. Actually, in the right-hand plot there are also two distinct Heun zeros, each one near the Bessel zero lying on the real axis, but the resolution is almost too low to see them as distinct.

observations concerning the cut profile $f_l(\chi;\rho_B)$ in (55). We mainly focus on the restricted parameter space $\mathbb{S}$ determined by $\rho_B \in [15, 25]$ and $0 \leqslant l \leqslant 10$, but also make mention of some remarkable features which crop up for other parameter values outside of this space. Our parameter space $\mathbb{S}$ has been chosen with the

following reasons in mind. First, its ρ_B interval is as discussed in the last paragraph. Second, it includes the first few values of l, which we want to single out for special attention. Third (and related to the first two), it avoids by design the aforementioned remarkable features. We stress that our discussion in this first subsection is mostly qualitative and amounts to a collection of conjectures without substantial numerical or analytical proof. Although we are bypassing a truly thorough study of some interesting phenomena, we do not believe these phenomena to be directly relevant for numerical implementation of ROBC (further remarks on this point to follow).

4.1.1. Zeros of the outgoing solution as a function of σ

Recall that in Section 3.1.3 we denoted by $\{k_{l,n} : n = 1, \cdots, l\}$ the zero set of the MacDonald function $K_{l+1/2}(z)$ which is also the zero set of $W_l(z)$. With this notation the zeros in σ of $W_l(\sigma\rho_B)$ are then simply the $k_{l,n}/\rho_B$. Let us collect several facts concerning such sets, summarizing results derived or listed in [19,22,54,55]. First, for even l these zeros come in complex-conjugate pairs, while for odd l they again come in complex-conjugate pairs save for a lone zero which lies on the negative $\mathrm{Re}\,\sigma$ axis. Second, the scaled zeros $(l+1/2)^{-1}k_{l,n}$ lie close to the asymptotic curve $\mathscr{C}$ introduced in Section 3.1.3. See Fig. 8 for a graphical demonstration of this claim. Hence, for each l one may imagine the zeros distributed in a crescent pattern in the lefthalf σ-plane. As concrete examples, the zeros of $W_2(15\sigma)$ are approximately $-0.1000 \pm \mathrm{i}0.0577$, while those of $W_3(15\sigma)$ are approximately $-0.1226 \pm \mathrm{i}0.1170$ and $-0.1548 + \mathrm{i}0$. Respectively, these zero sets are marked by crosses in the left-hand plots of Figs. 19 and 20.

Zeros for chosen parameter space. Dealing with $W_l(\sigma\rho_B;\sigma)$ as a function of σ in the Heun scenario, we have denoted the zeros of this function by $\sigma_{l,n} = \sigma_{l,n}(\rho_B)$. Over the range $\mathbb{S}$ of parameters mentioned above, the zeros $\sigma_{l,n}$ behave qualitatively similar to the zeros $k_{l,n}/\rho_B$ of $W_l(\sigma\rho_B)$, save for one key difference associated with odd l. Fig. 19 displays contour plots showing zero locations for $W_2(15\sigma;\sigma)$ and $W_2(25\sigma;\sigma)$.

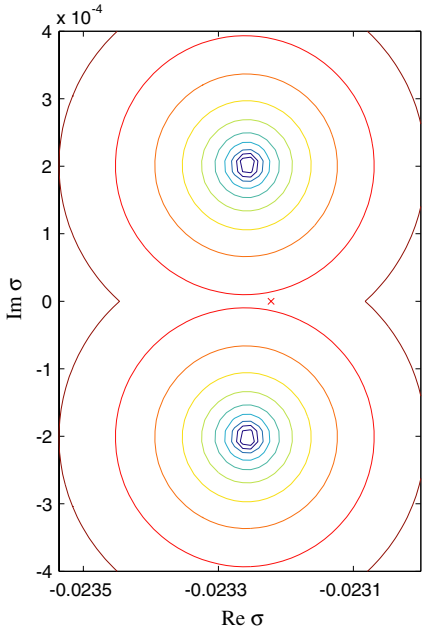

Fig. 21. Zeros of $W_3(100\sigma;\sigma)$. Here we plot contour lines of $\log|W_3(100\sigma;\sigma)|$. Note that two zeros of $W_3(100\sigma;\sigma)$ lie outside of the plot, as we focus on the pair of zeros closest to the real axis. The red cross is a zero of $W_3(100\sigma)$. We might gather from this plot that the feature associated with odd l and discussed in the text persists as ρ_B gets large.

Likewise, Fig. 20 displays contour plots showing zero locations for $W_3(15\sigma;\sigma)$ and $W_3(25\sigma;\sigma)$. These plots exhibit the main features associated with the zeros of $W_l(\sigma\rho_B;\sigma)$ over $\mathbb{S}$. To the eye, apparent zero locations in these plots nearly match zero locations (marked as crosses) for the corresponding Bessel functions. However, as shown in Fig. 20 and also noted in the figure caption, there is a key difference associated with odd l. To appreciate the difference, compare the zeros of $W_3(15\sigma)$ with those of $W_3(15\sigma;\sigma)$. Notice that the single zero of $W_3(15\sigma)$ lying on the negative $\mathrm{Re}\,\sigma$ axis corresponds to two zeros of $W_3(15\sigma;\sigma)$, one lying just above and the other just below the negative $\mathrm{Re}\,\sigma$ axis. This is a generic feature belonging to all odd values of $l \in \{1,\ldots,9\}$ and $\rho_B \in [15,25]$ considered here. Therefore, for the Heun scenario and the parameter space $\mathbb{S}$ at hand there are an even number of zeros whether l is even or odd. Moreover, we believe that this feature (of a pair of complex-conjugate zeros lying close to the real axis and together corresponding to a single Bessel zero) persists as ρ_B gets large, as evidenced by Fig. 21 and its caption. More precisely, if $N_l = N_l(\rho_B)$ denotes the number of zeros belonging to $W_l(\sigma\rho_B;\sigma)$, then for each $l \in \{0,\ldots,10\}$ we observe that N_l is constant on $[15,25]$ with $N_0 = 0$, $N_1 = 2 = N_2$, $N_3 = 4 = N_4$, $N_5 = 6 = N_6$, $N_7 = 8 = N_8$, and $N_9 = 10 = N_{10}$. Our conjecture is that each N_l is also the same constant on $[15,\infty)$.

Asymptotics of zeros. We discuss two asymptotic regimes for zero locations: one large ρ_B at fixed l and the other large l at fixed ρ_B. Turning to the first regime, we conjecture that the zeros $\sigma_{l,n}(\rho_B)$ approach the Bessel zeros $k_{l,n}/\rho_B$ as ρ_B becomes large. That is to say, the first term in the asymptotic expansion (53) is

$$\sigma_{l,n,1} = k_{l,n}. \tag{76}$$

Fig. 22 is a typical piece of graphical evidence indicating such behavior. Using the zero locations shown in this figure, we have confirmed for each n that $|\sigma_{10,n}(\rho_B) - k_{10,n}/\rho_B| = O(\rho_B^{-2})$ over $[15,25]$, in parallel with the first two terms in (53).

Now turning to the second asymptotic regime, we remark on the order scaling of Heun zeros as l becomes large. We have observed that the scaled zeros $(l+1/2)^{-1}\sigma_{l,n}$ tend to accumulate on the same fixed

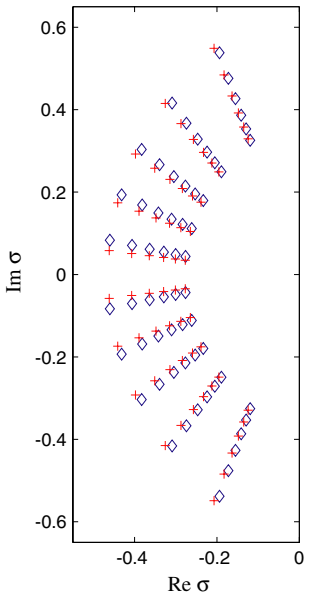

Fig. 22. Zeros of $W_{10}(\sigma\rho_B;\sigma)$ and $W_{10}(\sigma\rho_B)$. Here we plot zeros of these functions for $\rho_B = 15,17,19,21,23,25$. The outermost crescent of diamonds are the zeros of $W_{10}(15\sigma;\sigma)$, while the innermost crescent of diamonds are the zeros of $W_{10}(25\sigma;\sigma)$. The outermost crescent of crosses are the zeros of $W_{10}(15\sigma)$, while the innermost crescent of crosses are the zeros of $W_{10}(25\sigma)$.

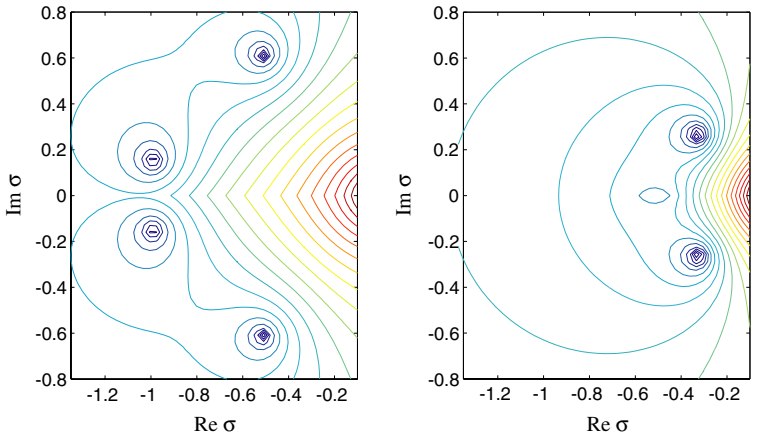

Fig. 23. Zeros of $W_2(\sigma\rho_B;\sigma)$. On the left we have a plot of $\log|W_2(2\sigma;\sigma)|$ and on the right one of $\log|W_2(4\sigma;\sigma)|$, demonstrating that a new pair of zeros is created between $\rho_B = 4$ and $\rho_B = 2$. The initial stages of this creation are perhaps evident in the rightmost plot.

Table 3
Approximate critical values of ρ_B

l	0	1	2	3	4	5	6	7	8	9	10
$\rho_B^{c_1}$	1.49	1.52	2.52	2.06	3.81	2.67	5.11	3.31	6.44	3.97	7.75
χ^{c_1}	0.63	1.31	0.79	1.49	0.85	1.60	0.89	1.67	0.91	1.71	0.92

Here we list rough values corresponding to the creation of the first new zero pair for $W_l(\sigma\rho_B;\sigma)$. For example, as ρ_B is lowered from 1.5 to 1.48, the number N_0 of zeros for $W_0(\sigma\rho_B;\sigma)$ jumps from 0 to 2. We also list approximate values for the location $-\chi^{c_1}$ of each zero-pair creation, again with ± 0.01 error bounds.

curve $\mathscr{C}_{\rho_B}$ as l becomes large. For example, using the 20 scaled zeros $\sigma_{20,n}(15)/20.5$ to hint at a candidate $\mathscr{C}_{15}$, one finds that – to the eye at least – all scaled zeros for $l < 20$ lie on this curve. Of course $\mathscr{C}_{\rho_B}$ is of a different shape than the dilated curve $\mathscr{C}/\rho_B$, although choosing a still larger fixed ρ_B value yields better agreement between the two curves. That is to say, consistent with the first type of asymptotic behavior discussed, we have $\rho_B\mathscr{C}_{\rho_B} \to \mathscr{C}$ holding pointwise as $\rho_B \to \infty$. We are not confident that this order scaling is robust for very large l.

Zero pair creation as ρ_B approaches unity. We have claimed that over the ρ_B interval $[15, 25]$ Heun zero behavior is similar to Bessel zero behavior, save for the aforementioned curious feature concerning odd l. As mentioned, we believe our claim remains true over $[15, \infty)$ for all low l here of interest. However, as we now argue, the number N_l of zeros for a given l is not conserved as $\rho_B \to 1^+$. The behavior we have noticed is the following. [13]

For each value $l \in \{0, \ldots, 10\}$ there is a critical value $\rho_B^{c_1}$ of ρ_B (less than 15 of course) for which a new pair of zeros is created on the negative $\mathrm{Re}\,\sigma$ axis, the branch cut. Below that there is yet another critical value $\rho_B^{c_2}$ for which yet another new pair of zeros is created on the negative $\mathrm{Re}\,\sigma$ axis, and so on. Therefore, it would seem that as a function $N_l(\rho_B)$ is step-like and blows up as $\rho_B \to 1^+$. Let us remark on the nature of the zero lying on the branch cut for a critical value $\rho_B^{c_j}$. As ρ_B is increased past $\rho_B^{c_1}$, say, two zeros appear to collide on the branch cut. However, they do not merge into a double zero, rather they pass "over and under each other", with each zero remaining on its own analytic neighborhood continued across the branch cut.

[13] The Heun zeros under consideration are analogous to the "flatspace quasinormal modes" discussed in the introduction of [57] by Nollert and Schmidt. As argued in Section 2.4.3, they are not the characteristic quasinormal modes of the blackhole.

In Fig. 23 we document the creation of the first new zero pair for $W_2(\sigma\rho_B;\sigma)$ associated with decreasing ρ_B from 4 down to 2. In Table 3 we have listed approximations to the critical values $\rho_B^{c_1}$ for $l \in \{0,\ldots,10\}$. Using $\sigma = \chi\exp(i\pi)$ along the negative $\mathrm{Re}\,\sigma$ axis, the table also lists approximate values for the location χ^{c_1} of each zero-pair creation. We have obtained these numbers using the method discussed below in reference to Fig. 26. All of the approximate critical values in the table are well below our ρ_B interval $[15,25]$; however, for higher l values creation of a zero pair can occur in our interval. For instance, in what follows we determine that creation of the first new zero pair for $l = 22$ occurs for $\rho_B^{c_1} \simeq 15.70$ and $\chi^{c_1} \simeq 0.96$.

4.1.2. Parameter dependence of the cut profile

Let us now discuss the cut profile $f_l(\chi;\rho_B)$ appearing in the representation (55) of the FDRK. We first remark on the behavior of the profile over the chosen parameter range $\mathbb{S}$, and then turn to exceptional behavior associated with critical parameter values lying outside $\mathbb{S}$.

Behavior over the chosen parameter range. For $0 \leqslant l \leqslant 10$ and for $\rho_B = 15$ and 25 we plot scaled even profiles in Fig. 24 and scaled odd profiles in Fig. 25. The scaling allows us to view all profiles on the same plot. Notice that the order-scaling is different for even and odd cases. As ρ_B is increased towards 25, the other endpoint of our interval, all of these profiles retain their shape; however, both their maximum value (in absolute value) and the essential window of their support vary.

Cauchy principal value. The chosen parameter space $\mathbb{S}$ has been carefully tailored to avoid the exceptional situation where a zero lies on the branch cut. However, over our ρ_B interval $[15,25]$, we shall of course be interested in l values higher than 10, and on this interval zero pair creation is an issue for such l. A glance at the form (63) of the cut profile $f_l(\chi;\rho_B)$ given earlier indicates that a negative real zero $\sigma = \exp(i\pi)\chi$ of $W_l(\sigma\rho_B;\sigma)$ should give rise to a singular cut profile.

For the aforementioned exceptional case $l = 22$ and $\rho_B^{c_1} \simeq 15.70$, we depict the profile blow-up in Fig. 26. In the top plot we have the cut profile $f_{22}(\chi;15.695964)$, where 15.695964 is approximately the critical value $\rho_B^{c_1}$ of ρ_B corresponding to the creation of the first new zero pair for the function $W_{22}(\sigma\rho_B;\sigma)$. For ρ_B values

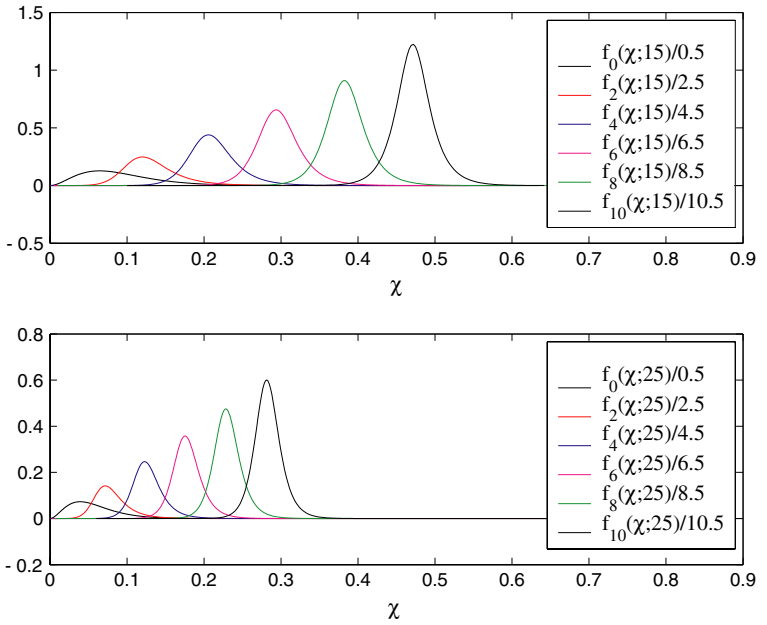

Fig. 24. Even cut profiles scaled by order for $\rho_B = 15$ and 25. Here, for example, $f_0(\chi;15)/0.5$ is on the far left, and $f_{10}(\chi;15)/10.5$ on the far right.

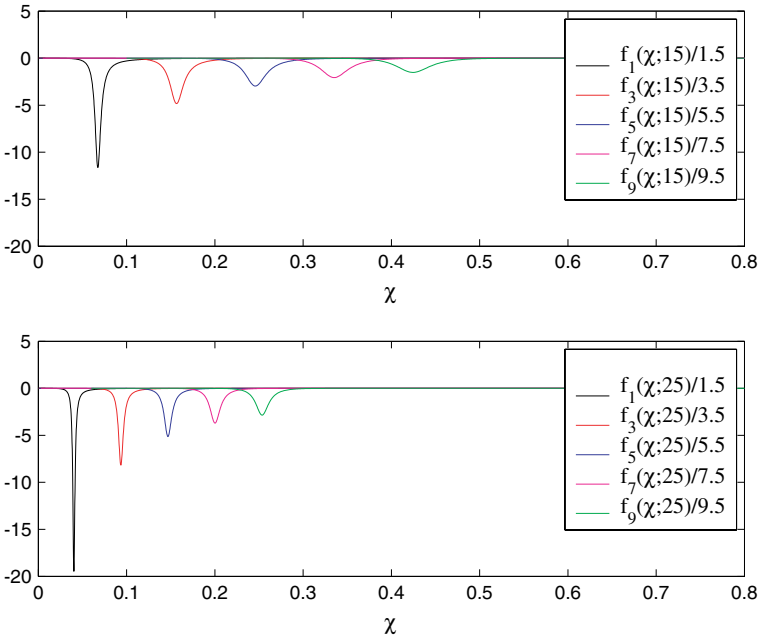

Fig. 25. Odd cut profiles scaled by order for $\rho_B = 15$ and 25. Here, for example, $f_1(\chi;15)/1.5$ is on the far left, and $f_9(\chi;15)/9.5$ on the far right.

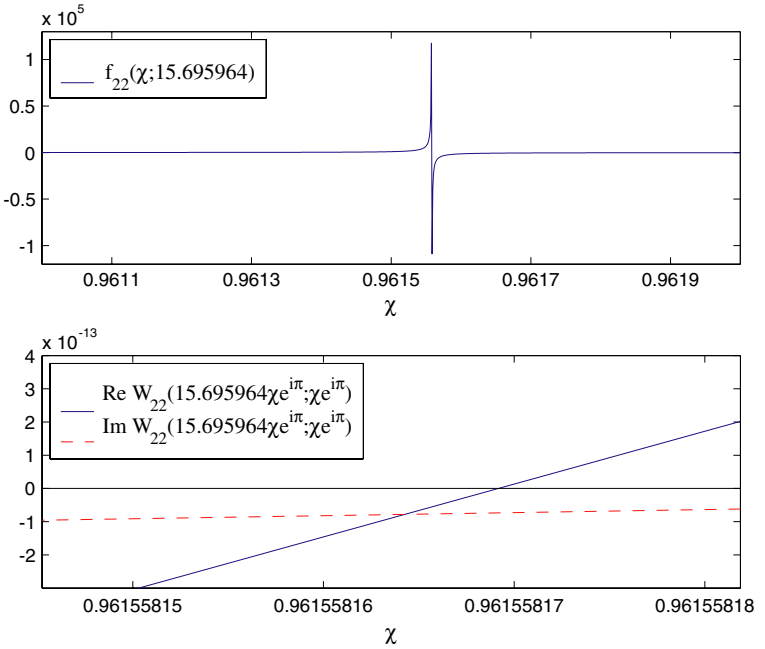

Fig. 26. Blow-up in cut profile near a critical value. The value 15.695964 is close to the critical value $\rho_B^{c_1}$ for $l = 22$. See the text for more description.

larger than $\rho_B^{c_1}$ the function has 22 zeros, but as ρ_B is lowered below $\rho_B^{c_1}$ a new pair of zeros appears from the branch cut. The lower plot depicts $\mathrm{Re}\, W_{22}(15.695964\sigma;\sigma)$ (solid line) and $\mathrm{Im}\, W_{22}(15.695964\sigma;\sigma)$ (dotted line) as well as their intersection point below the zero line. For $\rho_B = 15.695962$ this intersection point lies above zero, while for $\rho_B = 15.695966$ it lies below zero. As this intersection point appears to move smoothly with varying ρ_B, we conjecture the existence of a zero on the branch cut for a critical $\rho_B^{c_1}$ between $\rho_B = 15.695962$ and $\rho_B = 15.695966$ (actually we know it lies between $\rho_B = 15.695962$ and $\rho_B = 15.695964$). Our guess at the value, $\rho_B = 15.695964$, should be within 2×10^{-6} of the true $\rho_B^{c_1}$. Furthermore, we note that for ρ_B slightly above the critical value the profile $f_{22}(\chi;\rho_B)$ is a positive peak like one in Fig. 24, but as ρ_B is lowered past $\rho_B^{c_1}$ the profile transitions to a negative (and sharper) peak like one in Fig. 25.

Despite the blow-up discussed in the last paragraph, we emphasize that along the $\mathrm{Im}\,\sigma$ axis, the FDRK $\hat{\omega}_{22}(\mathrm{i}y;\rho_B)$ itself changes smoothly as ρ_B varies across $\rho_B^{c_1}$. Indeed, the pieces $\mathrm{Re}\,\hat{\omega}_{22}(\mathrm{i}y;\rho_B)$ and $\mathrm{Im}\,\hat{\omega}_{22}(\mathrm{i}y;\rho_B)$ may be computed either via the representation (55) or numerically via the methods outlined in Section 3.2. Using the latter methods, we observe that both pieces vary smoothly as ρ_B varies across the critical value $\rho_B^{c_1}$. We therefore offer the following conjecture. Although the cut profile $f_{22}(\chi;\rho_B)$ is singular at a particular point $\chi_{c_1} \simeq 0.96$ when $\rho_B = \rho_B^{c_1} \simeq 15.70$, the corresponding integral contribution

$$-\frac{1}{\pi}\int_0^\infty \frac{f_{22}(\chi;\rho_B)}{\mathrm{i}y+\chi}\,\mathrm{d}\chi \tag{77}$$

to $\hat{\omega}_{22}(\mathrm{i}y;\rho_B)$ varies smoothly as ρ_B varies across $\rho_B^{c_1}$. This would seem to indicate that $f_{22}(\chi;\rho_B^{c_1})/(\mathrm{i}y+\chi)$ has a distributional interpretation, and we believe its integral to be defined in the sense of Cauchy Principal Value. The nearly antisymmetrical blow-up in the top plot of Fig. 26 is in accord with this conjecture.

4.2. Numerical construction of the radiation kernel

We now document our numerical construction of the representation (55) over the chosen parameter space $\mathbb{S}$, also discussing in detail the accuracy of the construction.

4.2.1. Construction for chosen parameter space

To obtain the numerical kernel, we have used the one-component path method described in Section 3.1.3 both to obtain pole locations and strengths as well as the cut profile for certain parameter choices. Let us first discuss our treatment of the poles.

Construction of pole locations and strengths. Let a choice of $l \in \{0,\ldots,10\}$ remain fixed throughout this paragraph. We choose nine Chebyshev points $\{1/\rho_B^k : k = 0,1,\ldots,8\}$ on the interval $[1/25, 1/15]$. That is to say, the formula

$$2\xi_B^k = 0.7 + 0.04 + (0.7 - 0.04)\cos[\pi(2k+1)/(2n+2)] \tag{78}$$

determines the nine numbers $\xi_B^k = 1/\rho_B^k$. Our choice of nine Chebyshev points suffices for our purposes, although we make no claim that nine is the optimal number of points. Next, for each k we have used the secant algorithm to find the zero set $\{\sigma_{l,n}(\rho_B^k)\}$ of $W_l(\sigma\rho_B^k;\sigma)$. Then, at fixed l and n we interpolate each function $\sigma_{l,n}(\rho_B)$ by an eighth degree Chebyshev polynomial $T_{l,n}(1/\rho_B)$ in inverse ρ_B, so that this polynomial approximates $\sigma_{l,n}(\rho_B)$ on the interval $[15,25]$. On the same interval, we approximate the pole strengths $\alpha_{l,n}(\rho_B)$ by $T'_{l,n}(1/\rho_B)/\rho_B$, where here the prime $'$ denotes $\mathrm{d}/\mathrm{d}\xi_B$ differentiation.

Construction of the cut profile. Given any small positive η, say $\simeq 10^{-12}$, we assume the existence of corresponding finite integration limits, $\chi_{\min}$ (which may or may not be 0) and $\chi_{\max}$, such that the integral

$$-\frac{1}{\pi}\int_{\chi_{\min}}^{\chi_{\max}} \frac{f_l(\chi;\rho_B)}{\mathrm{i}y+\chi}\,\mathrm{d}\chi \tag{79}$$

approximates the true value

$$-\frac{1}{\pi}\int_0^\infty \frac{f_l(\chi;\rho_B)}{iy+\chi}\,d\chi \tag{80}$$

to within relative error η uniformly for $y \in \mathbb{R}$. We stress that this is an assumption, although one apparently true for the analogous cut profiles stemming from integral order ($\nu = l + 1/2 = n$) Bessel functions $W_{(n-1/2)}(\sigma\rho_B)$, as shown in the fourth section of [19]. In practice we have "eyeballed" the integration window $[\chi_{min}, \chi_{max}]$, for example referring to Fig. 3 of Section 2.4.2, we have chosen $[0.0005, 1.125]$ for $l = 2$ and $\rho_B = 15$. The correctness of our guess will be confirmed when we later examine the accuracy of the kernel. Finally, to obtain the cut contribution to the value $\hat{\omega}_l(iy;\rho_B)$ for a given y, we discretize the integral (79) via the Simpson rule. For the profile in the aforementioned figure we have used 1024 subintervals. Values $f_l(\chi_j;\rho_B)$ belonging to nodes χ_j in the corresponding discrete sum are computed with the one-component path method. Since for our chosen parameter range the considered profiles appear to be of definite sign, we expect that these sums are not plagued by cancellation error.

The foregoing construction of the cut contribution is applicable for a fixed value of ρ_B, whereas our construction for poles yielded locations and strengths over the whole ρ_B interval $[15, 25]$. To handle the cut contribution over the whole interval, we again introduce the Chebyshev points $\{1/\rho_B^k : k = 0, 1, \ldots, 8\}$, and – for each χ_j integration node – construct an eighth degree polynomial in $1/\rho_B$ which interpolates $f_l(15\chi_j/\rho_B;\rho_B)$. Notice that we are also scaling the integration nodes χ_j associated with $\rho_B = 15$ [and determined by the choice of χ_{min} and χ_{max} as well as the number of subintervals chosen to evaluate the integral (79) via Simpson's rule].

4.2.2. Accuracy of the construction

We check the accuracy of our numerical kernel in two ways, and as one result provide compelling numerical evidence that the FDRK indeed admits the sum-of-poles representation (55).

Value of the kernel at the origin. Building the pole and cut contributions to the kernel as described, we may compute a numerical value for $\hat{\omega}_l(0;\rho_B)$ and check it against the accurate series (75). We find that for *any* choice of l and ρ_B in $\mathbb{S}$ the numerical value for $\hat{\omega}_l(0;\rho_B)$ has absolute error less than 10^{-11} (in fact on the order of 10^{-12} or better). We stress that this level of accuracy holds even when $1/\rho_B$ is not a Chebyshev node, in which case the pole and the cut contributions to the kernel are obtained via interpolation.

Direct check. For $1 \leqslant l \leqslant 10$ we now have two independent numerical methods for evaluating the Heun FDRK $\hat{\omega}_l(iy;\rho_B)$. The first is evaluation of the numerical kernel directly constructed via the representation (55) as described in this subsection. The second is evaluation using path integration as described in Section 3.2. As a final and perhaps most convincing accuracy check, we compare these two methods. In Fig. 27 we have such a comparison for $\hat{\omega}_3(iy;15) = w_3(15iy;iy)$. With the two numerically obtained kernels we form an absolute error measure $|\Delta w_3(15iy;iy)|$ and a relative error measure $|\Delta w_3(15iy;iy)|/|w_{10}(15iy;iy)|$, where in forming the denominator of the relative error we happen to have used the directly constructed kernel. We plot these error measures in the figure. Over all of $\mathbb{S}$, save for $l = 0$ cases, this check indicates that we have relative and absolute errors better than 10^{-11}. As for $l = 0$, we believe the integration methods of Section 3.2 to be less reliable than the directly constructed kernel. Indeed, $\hat{\omega}_0(iy;\rho_B)$ is quite concentrated around the origin, and very small values of y negate the exponential error suppression built into the three-component integration method of Section 3.2.2. In any case, for $l = 0$ the first accuracy check of $\hat{\omega}_0(0;\rho_B)$ should be convincing in and of itself. Indeed, in the absence of a pole contribution to the kernel, one expects the largest error at the y-origin. Moreover, the largest error is indeed concentrated near the origin in other small-l plots such as those shown in Fig. 27. Via comparison with the series (75), we have found that our directly constructed numerical kernel yields a value for $\hat{\omega}_0(0;15)$ with an absolute error better than 7.5×10^{-13} and a relative error better than 2.2×10^{-11}.

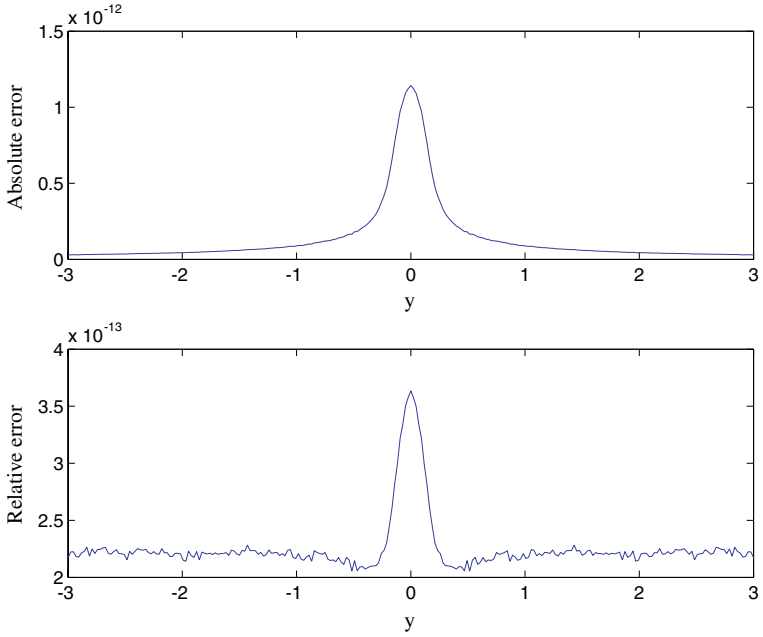

Fig. 27. Error in Heun FDRK $\hat{\omega}_3(\mathrm{i}y;15) = w_3(15\mathrm{i}y;\mathrm{i}y)$. With 256 y-subintervals we plot the errors, $|\Delta w_3(15\mathrm{i}y;\mathrm{i}y)|$ and $|\Delta w_3(15\mathrm{i}y;\mathrm{i}y)|/|w_3(15\mathrm{i}y;\mathrm{i}y)|$, described in the text.

5. Discussion

Our description of ROBC on the Schwarzschild geometry has been inspired by Alpert, Greengard, and Hagstrom's description for flatspace. Moreover, in order to implement the described conditions in an actual code (the results of which are reported in [1,2]), we have also based our implementation on the AGH technique of kernel compression. Namely, approximation of the FDRK by a proper rational function as commented on at the end of Section 2.4.2. Refs. [1,2,19,55] (with more detail in the latter three) describe the algorithm which produces the rational approximation, that is the numbers $\gamma_{l,n}$ and $\beta_{l,n}$ appearing in (57). Here we again emphasize that its use requires the ability to accurately evaluate the FDRK $\hat{\omega}_l(\mathrm{i}y;\rho_{\mathrm{B}})$ for $y \in \mathbb{R}$ (or at least for real y in some large window about the origin). We have developed numerical methods in this article precisely for use in the compression algorithm. With these considerations in mind, let us compare our work to that of AGH from theoretical and numerical standpoints.

From a theoretical perspective our work is less satisfactory than that of AGH, chiefly because, as it turns out in [2], we are unable to give a rigorous asymptotic analysis of our implementation, that is to say a description of the growth rate of d [the integer in (57)] in terms of order $\nu = l + 1/2$ and error tolerance ε. For each angular l index AGH deal with a Bessel FDRK which is theoretically known to admit a sum-of-poles representation, one corresponding to a purely discrete sum in the case of $3+1$ wave propagation and to a discrete and continuous sum in the $2+1$ case. Moreover, due to the exhaustively studied properties of Bessel functions, they also start with a wealth of useful information about how the pole locations, pole strengths, and (in the $2+1$ case) cut profile for the representation behave in all conceivable asymptotic regimes (which include certain scaling properties as l becomes large). With tight control over where the physical poles accumulate and the behavior of cut profile, they are able to borrow ideas from the fast-multipole method in order to replace (discrete and continuous) physical pole sums with (fully discrete) approximate pole sums of fewer terms. As a result, they rigorously prove that the sum-of-poles

representation for the Bessel FDRK admits a rational approximation, one uniformly valid in the righthalf frequency plane and exhibiting exponential convergence as the number of approximating poles is increased. For the scenario we have considered, such an analysis would seem out of the question. Indeed, although we have provided extremely convincing numerical evidence that the Heun FDRK admits a sum-of-poles representation, one strikingly similar to the $2+1$ Bessel case, even this is conjecture from a theoretical standpoint. The battery of asymptotics needed to theoretically prove that such a representation admits a rational approximation in the style of AGH is certainly well beyond this author's knowledge of special functions.

However, from a purely numerical standpoint we believe our work is closer to being on the same footing with that of AGH. Indeed, as seen in [1,2], insofar as *numerical* implementation of flatspace ROBC is concerned, their elegant asymptotic analysis proving the existence of rational approximations is somewhat beside the point. Ultimately, their compression algorithm (which yields the desired rational approximations) relies only on the ability to evaluate the Bessel FDRK along the imaginary axis of the frequency plane. For Bessel functions, which obey certain order recursion relations, such evaluation can be efficiently done via the continued fraction expression (62) following from such relations. We stress that such evaluation requires no knowledge of the sum-of-poles representation for the kernel. Although we have no such continued fraction expression with which to evaluate the Heun FDRK, we have seen that our integration method is almost as accurate (in the sense spelled out by Section 3.2.4). For Bessel kernels we have observed that the numerical path integration required by our method is more expensive than continued fraction evaluation, and all the more so as the order $l+1/2$ gets large, although we have not made a systematic comparison of the two methods. However, the cost of evaluation is almost beside the point, since in principle any extra cost associated with our method need only be incurred once. Of true importance is accuracy, and through the use of extended precision we believe it possible to evaluate Heun kernels through a bandwidth of 1024 and accurately enough to allow for rational approximation with $\varepsilon = 10^{-15}$, the best numbers reported by AGH. We point out that, insofar as both gravitational wave astronomy [60] and the post-Newtonian approximation [59,61] of the gravitational field are concerned, l values well below 64 are the ones primarily relevant to gravitational wave observation.

Acknowledgements

The material presented here has been drawn from [1], a 2003 Ph.D. dissertation in applied mathematics. I am grateful for the generous guidance of my academic advisor, Professor M.L. Minion. Beyond frequently helping me throughout the course of this project, he also carefully read multiple earlier drafts of my dissertation, offering many invaluable criticisms and suggestions for improvement. I also thank the other members of my Ph.D. dissertation committee: Professors C.R. Evans (UNC Physics & Astronomy), M.G. Forest, S. Mitran, and M.E. Taylor. Thanks also to both Doctors L. Lee and R. Zhou for helpful conversations and Professor T. Hagstrom (University of New Mexico) for email correspondence. I want to especially thank Professor C.R. Evans for crucial discussions (particularly early on) both about this problem and wave simulation on blackholes in general. Several key ideas in the work were developed during these discussions, and joint work with Professor Evans on this subject will appear elsewhere. I also acknowledge the influence of Professor M.E. Taylor, as well as encouragement and general support from both Professor Taylor and Professor J.M. Hawkins. For collaborations on other projects affecting this one, I thank Professor W. Kummer (Vienna Technical University), Professor A.N. Petrov (Moscow State University), and especially both Professors J.D. Brown (North Carolina State University) and J.W. York (Cornell University). I make special note of the lasting influence and inspiration of Professor York, under whose supervision I received a 1994 physics Ph.D. in general relativity.

References

[1] S.R. Lau, Rapid evaluation of radiation boundary kernels for time-domain wave propagation on blackholes, applied math Ph.D dissertation, UNC-Chapel Hill, December 2003. Available both at //www.unc.edu/~lau/" locator-type="url1">www.unc.edu/~lau/ and – in condensed form – at gr-qc/0401001.

[2] S.R. Lau, Rapid evaluation of radiation boundary kernels for time-domain wave propagation on blackholes: implementation and numerical tests, second half of gr-qc/0401001, Class. Quantum Grav., to appear.

[3] J.D. Brown, J.W. York, Quasilocal energy and conserved charges derived from the gravitational action, Phys. Rev. D 47 (1993) 1407.

[4] J.D. Brown, S.R. Lau, J.W. York, Action and energy of the gravitational field, Ann. Phys. 297 (2002) 175.

[5] E. Lindman, Free space boundary conditions for the time dependent wave equation, J. Comput. Phys. 18 (1975) 66–78.

[6] B. Engquist, A. Majda, Absorbing boundary conditions for the numerical simulation of waves, Math. Comp. 31 (1977) 629–651.

[7] B. Engquist, A. Majda, Radiation boundary conditions for acoustic and elastic wave calculations, Commun. Pure Appl. Math. 32 (1979) 313–357.

[8] B. Gustafsson, H.-O. Kreiss, Boundary conditions for time-dependent problems with an artificial boundary, J. Comput. Phys. 30 (1979) 333.

[9] A. Bayliss, E. Turkel, Radiation boundary conditions for wave-like equations, Commun. Pure Appl. Math. 33 (1980) 707–725.

[10] T. Hagstrom, Reduction of unbounded domains to bounded domains for partial differential equation problems, Ph.D. dissertation, California Institute of Technology, 1983.

[11] R. Kosleff, D. Kosleff, Absorbing boundaries for wave propagation problems, J. Comput. Phys. 63 (1986) 363–376.

[12] D. Givoli, Non-reflecting boundary conditions, J. Comput. Phys. 94 (1991) 1.

[13] I.L. Sofronov, Conditions for complete transparency on the sphere for the three-dimensional wave equation, Russian Acad. Sci. Dokl. Math. 46 (2) (1993) 397.

[14] J.-P. Berenger, A perfectly matched layer for the absorption of electromagnetic waves, J. Comput. Phys. 114 (1994) 185–200.

[15] M.J. Grote, J.B. Keller, On nonreflecting boundary conditions, J. Comput. Phys. 122 (1995) 231.

[16] M.J. Grote, J.B. Keller, Exact nonreflecting boundary conditions for the time dependent wave equation, SIAM J. Appl. Math. 55 (2) (1995) 280.

[17] M.J. Grote, J.B. Keller, Nonreflecting boundary conditions for time-dependent scattering, J. Comput. Phys. 127 (1996) 52.

[18] T. Hagstrom, Radiation boundary conditions for the numerical simulation of waves, Acta Numer. 8 (1999) 47–106.

[19] B. Alpert, L. Greengard, T. Hagstrom, Rapid evaluation of nonreflecting boundary kernels for time-domain wave propagation, SIAM J. Numer. Anal. 37 (2000) 1138.

[20] B. Alpert, L. Greengard, T. Hagstrom, Nonreflecting boundary conditions for the time-dependent wave equation, J. Comput. Phys. 180 (2002) 270.

[21] T. Hagstrom, New results on absorbing layers and radiation boundary conditions, 2003 (preprint).

[22] G.N. Watson, A Treatise on the Theory of Bessel Functions, second ed., Cambridge University Press, Cambridge, 1944.

[23] F.G. Friedlander, On the radiation field of pulse solutions of the wave equation, Proc. Roy. Soc. A 269 (1962) 53–65.

[24] J.A. Wheeler, Geons, Phys. Rev. 97 (1955) 511.

[25] T. Regge, J.A. Wheeler, Stability of a Schwarzschild singularity, Phys. Rev. 108 (1957) 1063.

[26] F.J. Zerilli, Gravitational field of a particle falling in a Schwarzschild geometry analyzed in tensor harmonics, Phys. Rev. D 2 (1970) 2141.

[27] S. Chandrasekhar, Mathematical Theory of Black Holes, Oxford University Press, Oxford, 1992.

[28] J.W. York Jr, in: L.L. Smarr (Ed.), Kinematics and Dynamics of General Relativity, Sources of Gravitational Radiation, Cambridge University Press, Cambridge, 1979.

[29] H. Friedrich, G. Nagy, Commun. Math. Phys. 201 (1999) 619.

[30] N.T. Bishop, R. Gómez, L. Lehner, J. Winicour, Cauchy-characteristic extraction in numerical relativity, Phys. Rev. D 54 (1996) 6153–6165.

[31] N.T. Bishop, R. Gómez, L. Lehner, M. Maharaj, J. Winicour, High-powered gravitational news, Phys. Rev. D 56 (1997) 6298–6309.

[32] M.E. Rupright, A.M. Abrahams, L. Rezzolla, Cauchy-perturbative matching and outer boundary conditions I: methods and tests, Phys. Rev. D 58 (1998) 044005.

[33] L. Rezzolla, A.M. Abrahams, R.A. Matzner, M.E. Rupright, S.L. Shapiro, Cauchy-perturbative matching and outer boundary conditions: computational studies, Phys. Rev. D 59 (1999) 064001.

[34] S.R. Lau, Outer boundary as arrested history in general relativity, Class. Quantum Grav. 19 (2002) 2853, Corrigendum, Class. Quantum Grav. 20 (2003) 1415.

[35] B. Szilágyi, B. Schmidt, J. Winicour, Boundary conditions in linearized harmonic gravity, Phys. Rev. D 65 (2002) 064015.

[36] J. Novak, S. Bonazzola, Solving wave equations with spectral methods and nonreflecting boundary conditions, gr-qc/0203102.

[37] G.B. Cook, S.A. Teukolsky, Numerical relativity: challenges for computational science, Acta Numer. 8 (1999) 1–45.

[38] E.W. Leaver, Spectral decomposition of the perturbation response of the Schwarzschild geometry, Phys. Rev. D 34 (1986) 384.
[39] N. Andersson, Evolving test fields in a black-hole geometry, Phys. Rev. D 55 (1997) 468.
[40] P.M. Morse, H. Feshbach, in: Methods of Theoretical Physics, vols. 1 and 2, McGraw-Hill, New York, 1953.
[41] A. Ronveaux (Ed.), Heun's Differential Equations, Oxford University Press, Oxford, 1995.
[42] S.Y. Slavyanov, W. Lay, Special Functions: a Unified Theory Based on Singularities, Oxford University Press, Oxford, 2000.
[43] A.H. Wilson, A generalized spheroidal wave equation, Proc. R. Soc. Lond. A 118 (1928) 617.
[44] E.W. Leaver, Solutions to a generalized spheroidal wave equation: Teukolsky's equation in general relativity, and the two-center problem in molecular quantum mechanics, J. Math. Phys. 27 (1986) 1238.
[45] C.W. Misner, K.S. Thorne, J.A. Wheeler, Gravitation, Freeman, San Francisco, 1973.
[46] M.E. Taylor, Partial Differential Equations, vol. III, Springer, New York, 1997.
[47] M.D. Greenberg, Advanced Engineering Mathematics, Prentice-Hall, Englewood Cliffs, NJ, 1988.
[48] J.J. Duistermatt, F.A. Grünbaum, Differential equations in the spectral parameter, Commun. Math. Phys. 103 (1986) 177.
[49] C.M. Bender, S.A. Orszag, Advanced Mathematical Methods for Scientists and Engineers, McGraw-Hill, New York, 1978.
[50] P.K. Chattopadhyay, Mathematical Physics, New Age International Ltd., New Delhi, 1990, p. 149.
[51] L.J. Slater, Confluent Hypergeometric Functions, Cambridge University Press, Cambridge, 1960.
[52] A.R. Curtis, Coulomb Wave Functions, Royal Soc. Math. Tables, vol. 11, University Press, Cambridge, 1964.
[53] I.J. Thompson, A.R. Barnett, Coulomb and Bessel functions of complex arguments and order, J. Comput. Phys. 64 (1986) 490.
[54] F.W.J. Olver, Asymptotics and Special Functions, Academic Press, New York and London, 1974.
[55] S. Jiang, Fast evaluation of nonreflecting boundary conditions for the Schrödinger equation, New York University Ph.D. Dissertation, 2001.
[56] K.D. Kokkotas, B.G. Schmidt, Quasi-normal modes of stars and black holes, Living Reviews of Relativity, gr-qc/9909058.
[57] H.-P. Nollert, B.G. Schmidt, Quasinormal modes of Schwarzschild black holes: defined and calculated via Laplace transformation, Phys. Rev. D 45 (1992) 2617.
[58] K.E. Atkinson, Elementary Numerical Analysis, second ed., Wiley, New York, 1993.
[59] K.S. Thorne, Multipole expansions of gravitational radiation, Rev. Mod. Phys. 52 (1980) 299.
[60] B.F. Schutz, Gravitational wave astronomy, Class. Quantum Grav. 16 (1999) A131.
[61] L. Blanchet, On the multipole expansion of the gravitational field, Class. Quantum Grav. 15 (1998) 1971.